Polyhedron 170 (2019) 334–358

Contents lists available at ScienceDirect

Polyhedron

journal homepage: www.elsevier.com/locate/poly

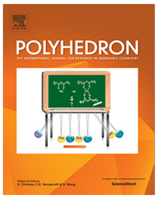

WWMOD? What would metal oxides do?: Redefining their applicability in today's energy technologies

Laura Flannery [a], Heilly Gálvez [b], Wendy Nimens [a], Ajara A. Rahman [a], Luisa Whittaker-Brooks [a,*]

[a] *Department of Chemistry, University of Utah, 315 South 1400 East, Salt Lake City, UT, United States*
[b] *Department of Chemical Engineering, University of Utah, 315 South 1400 East, Salt Lake City, UT, United States*

ARTICLE INFO

Article history:
Received 25 April 2019
Accepted 3 June 2019
Available online 14 June 2019

Keywords:
Metal oxides
Characterization
Solar cells
Braggs reflectors
Synthesis
Plasmonics
Electronic properties

ABSTRACT

What would metal oxides do?: To answer this question, we will have to focus on the nature of the metal–oxygen bond as it can vary between being ionic, highly covalent, or metallic. The distinctive variety of electronic, optical, and magnetic properties (i.e., accessible electronic transitions, high dielectric constants, wide bandgaps, tunable electrical and thermal conductivities) often encountered in metal oxides are clearly due to the unique nature of their outer *d*-electrons. Given all conceivable metal oxide combinations, we may find that it is possible to yield structures with unique metallic (i.e., ReO_3, RuO_2, $LaNiO_3$), semiconducting (i.e., ZnO, TiO_2), and insulating (i.e., $BaTiO_3$, Al_2O_3, SiO_2) properties. Strongly correlated metal oxides may also undergo metal-to-insulator phase transitions (i.e., V_2O_3, VO_2, $La_{1-x}Sr_xVO_3$) which allow us to further tune their electronic properties. Strongly correlated metal oxides may also demonstrate charge density wave (i.e., $K_{0.3}MoO_3$), defect ordering (i.e., $Ca_2Mn_2O_5$, $Ca_2Fe_2O_5$), ferromagnetism (i.e., Fe_3O_4, CrO_2, $La_{0.5}Sr_{0.5}MnO_3$), and antiferromagnetism (i.e., NiO, $LaCrO_3$) properties. Given their versatile optical and electronic activity, metal oxides have been extensively investigated as key components in optics, electrochemistry, photocatalysis, plasmonics, and photovoltaics. Understanding the structural, morphological, and optoelectronic properties of either naturally occurring or synthetically fabricated metal oxides provides a pathway for the development of novel metal oxides with properties that can be tuned to fulfill the efficiency demands of a particular application. Here, we present a comprehensive review of the synthesis, characterization tools, and applications of metal oxide nanostructures and their thin films. We will also discuss the synthesis, characterization, and applications of metal oxide heterostructures. We have wittingly narrowed the scope of this review to only include the use of metal oxides for energy conversion applications. Finally, we will provide our fair assessment on the outlook, challenges, and opportunities we foresee in metal oxides research and applications.

1. Overview

The semiconductor industry has been built around devices using silicon as the key material. This semiconductor is at the heart of most commercial thin-film transistors, light-emitting diodes, and photovoltaics. While silicon is a widely used and very effective semiconductor, there are many drawbacks associated with the material including rigidity, lack of transparency, and, most importantly, laborious fabrication steps when incorporated into devices. To mitigate these challenges, the semiconductor industry has turned to amorphous silicon (a-Si) which may be processed at lower temperatures and is, therefore, less expensive than crystalline silicon. In addition, a-Si can be deposited onto flexible substrates that require low-temperature processing. However, a-Si has lower mobility than those observed in crystalline silicon. Thin film metal oxides offer a viable alternative to silicon and have proven highly efficient in many optical and electronic devices. Many metal oxides have much larger carrier mobility values when compared to that of a-Si ($0.5–1\ cm^2\ V^{-1}\ s^{-1}$), with single crystalline metal oxides exhibiting mobility values in the range of $\approx 100\ cm^2\ V^{-1}\ s^{-1}$ [1,2]. Metal oxides have high transmittance in the visible region, making them excellent candidates as charge transport layers in electronic devices. In addition to mobility and transparency, metal oxides may be processed at low temperatures, enabling their use in organic electronics and their deposition on flexible, plastic substrates for electronics with high form factors. Processing conditions and post-processing treatments may have a significant effect on crystallinity, mobility, and energy level alignment of metal oxides. With many processing methods readily available and inexpensive,

---

* Corresponding author.
E-mail address: luisa.whittaker@utah.edu (L. Whittaker-Brooks).

https://doi.org/10.1016/j.poly.2019.06.001
0277-5387/

metal oxides provide a unique opportunity to tailor material properties to a certain function within a device. Here, we examine structure–property–function relationships of metal oxides, modified by processing and post-processing chemistry. We will also discuss how metal oxides are used in energy conversion applications.

2. Synthesis strategies for the fabrication of metal oxide nanostructures and thin films

Great progress has been achieved in the fabrication of metal oxides with the rapid development of material design strategies and synthesis techniques. Especially now, there is a wealth of chemical and physical methodologies developed to prepare nanostructured metal oxides with improved crystallinity. To date, most metal oxide powders are fabricated by sol–gel [3], precipitation [4], decomposition [5], hydrothermal [6], and template-assisted synthesis [7] strategies while thin films are normally assembled either by Langmuir-Blodgett, chemical bath, electrochemical deposition, inkjet printing, spray-, spin-, and dip-coating processes or by more laborious processes involving vapor and molecular vapor vacuum deposition techniques (Fig. 1) [8–13]. From the strategies used for synthesizing metal oxide nanoparticles, sol–gel and hydrothermal synthesis strategies provide facile fabrication protocols that do not rely on expensive equipment, high vacuum, or high temperatures. These synthesis protocols also yield metal oxide nanoparticles with tunable morphologies (i.e., spheres, rods, wires, etc.). However, for the large-scale synthesis of metal oxide nanoparticles, chemical precipitation strategies are often preferred. The reactions involved are also much simpler than those in other solution-based synthesis techniques. For chemical precipitation to occur, it is necessary that the concentration of one of the reactants (normally a solid) be above the solubility limit of the host. A solid will then form due to rapid quenching or ion implantation, and if the temperature is high enough that diffusion can

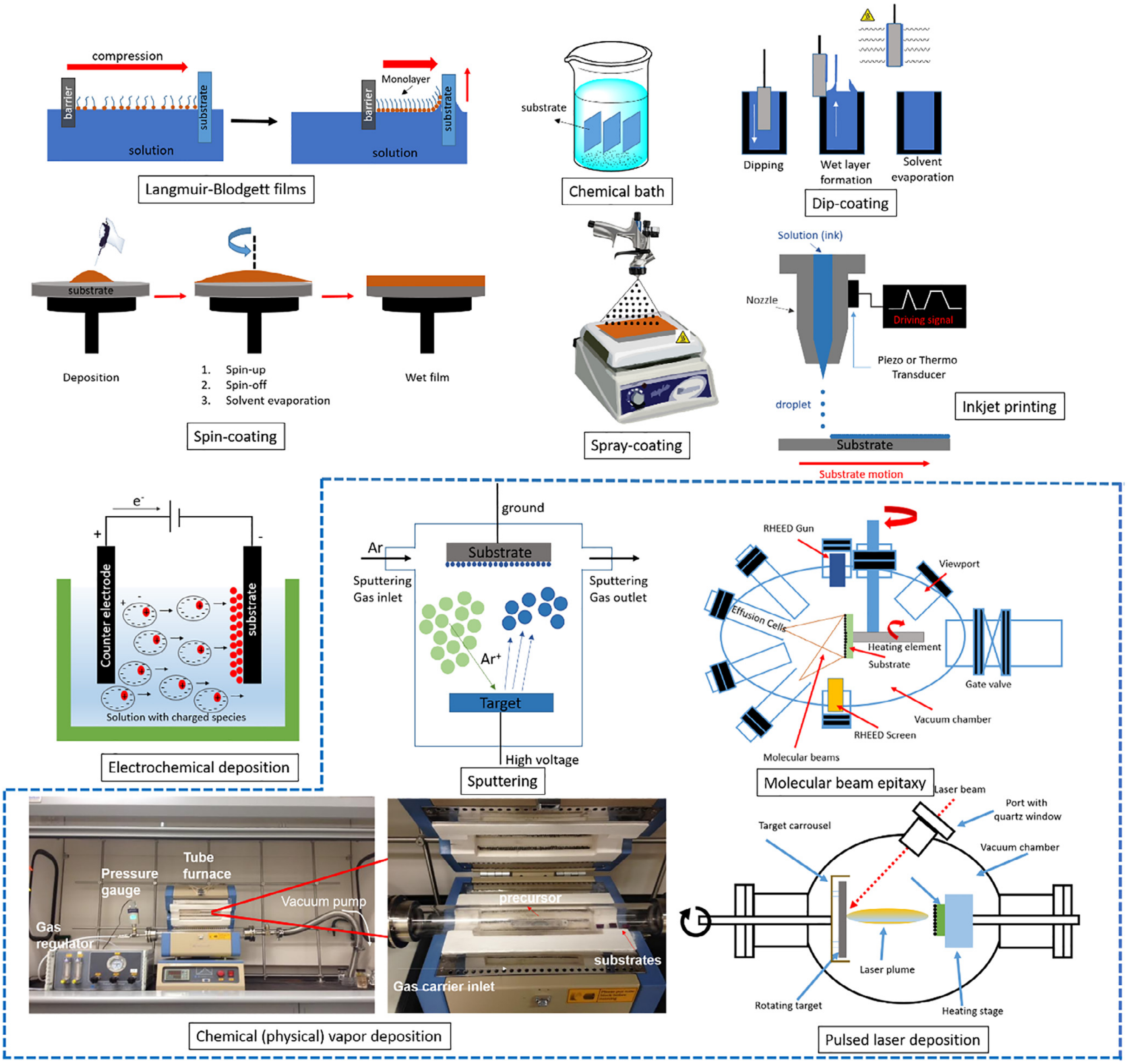

Fig. 1. Deposition techniques (vacuum-based techniques are denoted inside the dashed blue box) developed for the fabrication of metal oxide nanostructures and thin films. (Colour online.)

lead to segregation into precipitates. Chemical precipitation is very fast with the whole reaction only requiring several minutes to complete the synthesis and does not require high temperatures. However, the major disadvantage of using a chemical precipitation synthesis process for the fabrication of metal oxide nanoparticles is the difficulty involved in precisely controlling the morphology of the product due to fast precipitation. In the case of sol–gel synthesis, microparticles or molecules in a solution agglomerate and under controlled conditions will eventually link together to form a network. Two variants of the sol–gel process stemming from the precursors used in the reaction are readily utilized. The first is dubbed the colloidal method and typically uses water as the solvent for suspending or dissolving the precursors. The second is called the polymeric or alkoxide method, where an alcohol is often used as the liquid for suspension or for dissolving the precursors (Fig. 2). Sol–gel processes may be complemented with spin- and dip-coating techniques to form a metal oxide thin film. When fabricating a thin film via spin-coating, the substrate, fixed to a stationary holder, is coated with a precursor solution. The substrate is then rotated at high speed and the coating is spread into a thin film by centrifugal force. The spin-coating time, speed, and acceleration can be adjusted to vary the thickness and quality of the film according to the viscosity and volatility of the solvent, as well as the metal oxide concentration in the solution [2]. Similarly, dip-coating allows for the growth of a metal oxide film by immersion of the substrate in a solution containing the particles to be deposited and subsequent withdrawal. Next, the adhered solution forms a film, which solidifies as the solution drains, evaporates, hydrolyzes, and reacts with its surroundings. A final curing step may further stabilize and induce crystallinity of the coating [14]. Another common and inexpensive method to cast metal oxides into thin films is spray, or cold spray, coating. Here, films are typically grown by misting a precursor solution over a preheated substrate [15]. Although the coating quality is usually inferior to those obtained via spin- or dip-coating methods, spray coating parameters can be adjusted to improve the roughness and porosity of the resulting film [2]. Finally, inkjet printing, specifically in the context of electronics, is a materials deposition method where metal oxide nanoparticles are patterned onto a substrate in well-defined shapes which can be integrated into an electronic circuit [16]. Inkjet printing is an additive, low-temperature process. For this reason, the usage of material and energy is minimized, and modifications to the pattern can be easily achieved [2]. One common way to synthesize metal oxide nanoparticle inks for printing is by the precipitation of metal acetates with the addition of a base. An organic ligand is often added to control the particle size. After ink-jet printing, thermal curing is required to remove the ligand [17].

As mentioned above, we can also use more expensive and laborious vacuum deposition processes such as vapor deposition (chemical; CVD and physical; PVD), pulsed laser deposition (PLD), sputtering, and molecular beam epitaxy (MBE) to yield metal oxide thin films. In contrast to many solution processes, vacuum-vapor deposition techniques yield metal oxide thin films with well-controlled stoichiometry, dimension, and high purity. For CVD, a precursor (which can be comprised of single or multiple reactive components) is vaporized and moved downstream a reaction chamber with the help of a carrier gas. The carrier gas is usually an inert gas, such as nitrogen or argon [18]. Chemical reactions (either with multiple reagents or single precursor decomposition) will occur in the vapor phase and due to the formation of a temperature gradient, a product will condense on a substrate located on the cool side of the chamber. Conveniently, any byproducts (usually gases or lightweight molecules) and unreacted precursors are exhausted out of the chamber. An important factor to consider when using CVD to fabricate metal oxide films deals with selecting an appropriate precursor that is volatile enough so that vaporization is attainable at a lower temperature than that required for chemical reactions to take place [19]. As such, CVD precursors do not necessarily have to be made into a solution. They can, alternatively, come in the form of volatile organometallic complexes of the metal or metal oxide to be deposited. Organometallic compounds are, in general, highly volatile and have relatively high reaction rates since the coordination of the metal–carbon bond is weaker than the covalent bonds in these molecules. For this reason, they are favored as precursors for CVD [20]. Even though metal–organic chemical vapor deposition (MOCVD) reactions can be kinetically (as opposed to thermodynamically) controlled; many difficulties that could arise from trying to completely remove the ligands. Research efforts are focused on developing and understanding the chemical reactivity of high molecular weight volatile compounds containing hard-soft chelating ligands that can be used

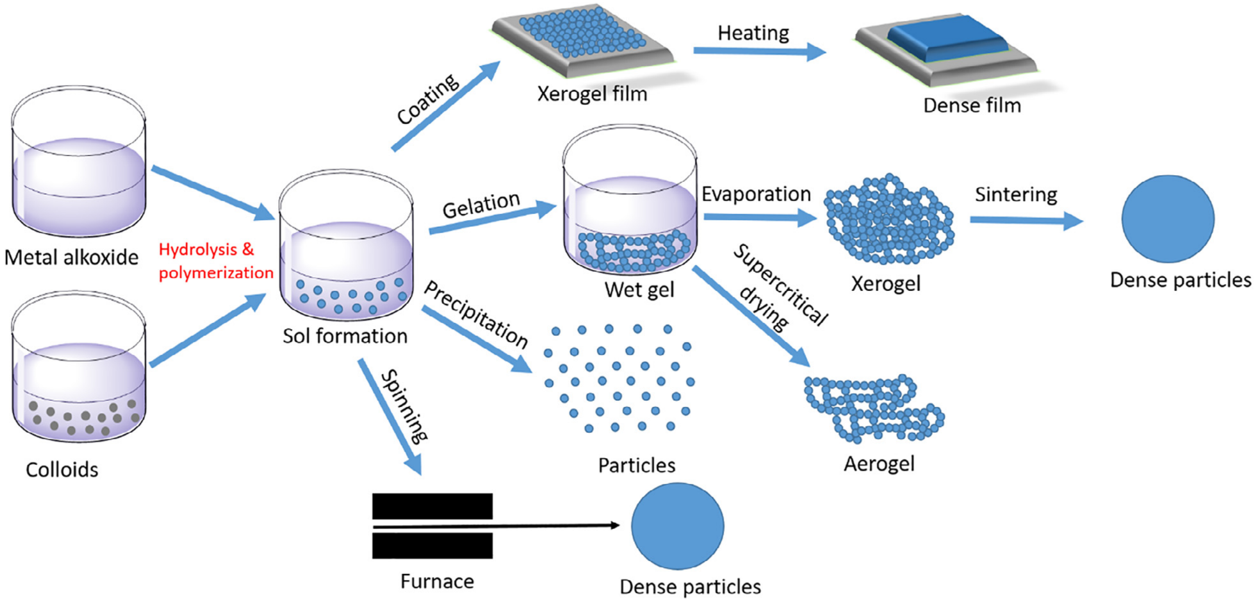

Fig. 2. Schematic depiction of the various reaction and processing steps involved in the sol–gel deposition process.

as precursors for the deposition of metal oxides [21–23]. Sputtering is another vacuum fabrication technique used for depositing metal oxide films. In this technique, an ionized inert gas is bombarded at the precursor which then collides with the substrate. A commonly used type is magnetron sputtering, where magnets are placed behind the target substrate to optimize the uniformity and rate of the deposition [2]. Some advantages presented by using sputtering to fabricate metal oxides include room temperature film deposition, compatibility with temperature-sensitive substrates, and better control over deposition parameters, which translate to a more defined metal oxide morphology. Pulsed laser deposition (PLD) is another versatile tool used to grow thin films. One of the main advantages it presents is stoichiometric transfer. In PLD, the precursor is efficiently evaporated and the target is irradiated with a high-power pulsed ultraviolet laser beam and a plasma plume deposits the material onto the target. PLD can be used to create metal oxide thin films with superior quality and performance when compared to other high-energy methods, but poses layer uniformity limitations when employed in large scales [2]. Similar to CVD, atomic layer deposition (ALD) is a method often used to grow metal oxides, however, reagents are not introduced simultaneously, but gaseous precursors are added sequentially in alternating pulses [2]. During the ALD process, each precursor is pulsed into a vacuum chamber and allowed to react with the substrate until exactly one complete monolayer is formed. Some advantages are the enhanced control over film composition and the moderate temperatures required [24]. Molecular beam epitaxy (MBE) is used for the precise synthesis of films of metals, semiconductors, and insulators. Chemical reactions between a high-temperature substrate under vacuum and molecular beams of the precursor cause layers of material to crystallize. The composition of these films can be controlled by tuning the collision rates of the reagents. The ability to control deposition fluxes allows for smooth layers to be formed when compared to other vacuum deposition methods [25]. Several beams can be arranged to target the substrate. Film thickness uniformity will depend on the geometrical configuration and molecular fluxes of the beams [25]. As presented, there is a vast array of deposition methods and techniques that could be used to synthesize metal oxide powders and thin films. As discussed later, all these processes may yield particles and films with various morphologies with unique electronic features.

3. Characterization techniques used in determining the morphology and electronic properties of metal oxide nanostructures and thin films

When considering the properties of metal oxides, three main categories of characterization should be considered, i.e., optical, electrical, and physical. Several spectroscopic tools such as ellipsometry, photoluminescence (PL), ultraviolet visible spectroscopy (UV–Vis), and reflectance are often utilized to characterize the optical properties of metal oxides. These methods tend to be non-destructive which is advantageous for preserving the integrity of the sample. The bandgap, for example, is an important optical parameter and in most metal oxides is in the range of 2–6 eV. UV–Vis absorption spectroscopy can be a simple technique to determine a materials optical bandgap; however due to structural defects and dangling surface bonds, new energetic states could appear in the bandgap of metal oxides, known as Urbach tail states [26]. These Urbach tail states create a nonlinear distribution of defect states within the bandgap upon the widening of the absorption edge. UV–Vis absorption spectroscopy can also be used as a tool to monitor the reduction of these defects states as a function of processing. For example, the optical bandgap of Cu_2O thin films is determined to increase from 2.38 to 2.51 eV after successfully reducing the Urbach energy upon annealing [27]. PL spectroscopy can provide information on structural defects because the photo-induced electrons and holes, if captured at defect sites, will recombine with light emission and the energy of emitted light will always be lower than the energy of absorbed light. By performing temperature-dependent PL measurements, activation energies using various PL emission peaks in metal oxides can also be determined [28–31]. If the PL emission peak originates from a defect, then the calculated activation energy will instead correspond to the ionization energy of the defect. There is also time-resolved PL spectroscopy which can be used to determine the emission of a material as a function of time after excitation by a laser at a particular wavelength. This allows us to study how intrinsic and extrinsic defects affect the optoelectronic properties of metal oxides [32]. Other techniques such as ellipsometry, reflectance, and transmittance spectroscopies are only applicable for relatively smooth metal oxide thin films. The non-homogeneity nature of metal oxide nanostructure layers and scaffolds pose a challenge when using these techniques to understand optical properties and could lead to misguided information. Although optical spectroscopy can provide critical information about the optoelectronic properties of metal oxides, it should be used in conjunction with other methods of electrical and structural characterization so a proper explanation of experimental results can be concluded.

The primary electrical analytical tools used for characterization of metal oxide nanostructures and thin films include cyclic voltammetry, differential Hall Effect measurements, impedance spectroscopy, and two- or four-point probe measurements. These methods have been utilized to determine resistivity, carrier concentration and lifetime, mobility, contact resistance, depletion widths, interface states and defects, and Schottky barrier heights. It is important to note that, poor control over size distributions, defects, and morphology variations may affect the electrical characterization of metal oxides [33,34]. Therefore, electrical and structural characterizations should always be done in parallel. Analytical tools, such as scanning electron microscopy (SEM), atomic force microscopy (AFM), x-ray photoelectron spectroscopy (XPS), ultraviolet photoelectron spectroscopy (UPS), and x-ray diffraction techniques (XRD) can provide surface and bulk structural information. Optical microscopy techniques may provide real space imaging allowing for a relatively quick understanding of the topography, surface roughness or other surface structures such as pores or surface defects. These images, depending on the resolution required, are commonly used in combination with scattering studies [35]. Scattering techniques are used to investigate nanostructured surfaces and thin films, and for metal oxides specifically, grazing-incidence wide-angle X-ray scattering (GIWAXS) and grazing-incidence small-angle X-ray scattering (GISAXS) are commonly used (Fig. 3). By using these techniques, the surface, bulk, and substrate-film interfaces are all accessible for structure and morphology analyses upon varying the incidence angle. The observed patterns range from rings to spots, implying limited or no orientation to high orientation, respectively. Currently, these grazing incidence techniques are very sensitive to surface structures and morphologies for a large variety of metal oxide structures available. This is due to the wide range of length scales that can be probed by simply moving the two-dimensional detector. The different systems that can be studied range from assemblies of nanoparticles or nanowires to ordered molecular systems, down to atomic crystals [36].

The electronic structure of metal oxides can be probed by photoelectron spectroscopy. Specifically, UPS allows for the determination of the work function and binding energies of specific elements present. Moreover, the influence of bonds, defects and other morphological structures affecting the materials chemical environment can be monitored [37,38]. X-ray absorption fine

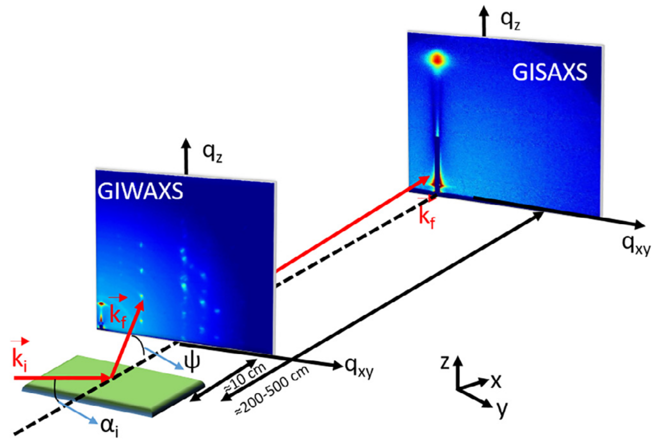

Fig. 3. Schematic representation of the scattering geometry using in GIWAXS and GISAXS studies. The different color intensities in both the GIWAXS and GISAXS spectra represent different scattering intensities on a logarithmic scale. Typical sample-to-detector distances are 10 cm and 200–500 cm for GIWAXS and GISAXS, respectively.

structure (XAFS) spectroscopy tools could also aid in providing a complete understanding of the electronic features of metal oxides. XAFS are typically divided into two regimes, X-ray absorption near-edge spectroscopy (XANES) and extended X-ray absorption fine-structure spectroscopy (EXAFS). The distinctions are convenient for the interpretation of results as XANES are strongly sensitive to changes in the formal oxidation state and coordination chemistry of the absorbing atom, while the EXAFS is used to determine the bond distances, coordination number and chemical species for neighboring atoms with respect to the absorbing atom. These techniques are especially useful for various oxide structures because they are equally successful for both ordered and disordered materials and sensitive to length scales down to a nanoparticle or even few molecules [39]. Although different strengths, challenges, accessibility, and limitations for each characterization tool (particularly, diffraction and spectroscopy tools) discussed in this review (and many others not discussed in this review) may arise, recent advances in their resolution and sensitivity are transforming the spatial precision and quantitative information that can be obtained on the structure, morphology, mechanical, magnetic, and optoelectronic features for the surface, the bulk, or a group of single atoms comprising a metal oxide. Furthermore, advances in the capabilities of current characterization tools have opened new research directions in the development of novel multifunctional metal oxide heterostructures with tunable properties that differ between the surface and bulk scale.

4. Assembly of metal oxide p-n heterojunctions

p-n heterojunctions are key building blocks for many semiconductor-based electronics such as field-effect transistors, light emitting diodes, photovoltaics, and thermoelectric devices. A heterojunction is an interface between two different materials and, in the case of p-n heterojunctions, is the boundary where an electron donor (p-type) comes into contact with an electron acceptor (n-type). It is at this interface where the majority of electronic events occur. Depending on the energy level alignment (and assuming no band bending) between the p- and n-type materials, three different types of heterojunctions may be possible, i.e., straddling gap (type I), staggered gap (type II), and broken gap (type III) [40]. Type II p-n heterojunctions being the most studied in electronics can easily promote charge transfer and separation at a particular interface which turns out to be beneficial for enhancing the efficiency of energy conversion devices [41]. In type II heterojunctions, the driving force for these events to occur is based on achieving equilibrium between an electron donor and acceptor at the interface. Therefore, we need to think about how energy level alignments are affected before and after the formation of the p-n heterojunction. Fig. 4 depicts a cartoon showing the charge transfer mechanism between p- and n-type materials before and after being in contact. Before contact (Fig. 4A), the Fermi level of the p-type material is close to the valence band (VB) and that of the n-type is located near the conduction band (CB). In the p-n heterojunction, the VB of the p-type is farther away from vacuum whereas the CB of the n-type materials is closer to vacuum. Consequently, electrons tend to diffuse from the CB of the p-type material into the CB of the n-type material. Upon the p- and n- materials being in contact, the energy levels of the p-type material shift upward along with the Fermi level, whereas those of the n-type material shift downward along with the Fermi level until equilibrium is reached. This results in the formation of a charged region, dubbed as the depletion region, where an electric field is generated due to charge density building up on either side of the interface. At this depletion region is where charge separation occurs and is often accompanied by band bending (Fig. 4B) [42,43].

As an integral component in semiconductor technologies, extensive research has been performed to expand the applicability of metal oxide nanostructures towards applications where p-n heterojunctions are utilized. To date, multi-segment, core–shell, bilayer, branched, and cross stacked structures with specific functionalities have been reported (Fig. 5) [44–47]. For example, bilayer and core–shell systems, intended to mimic thin film bilayers, are utilized to maximize the interface between the p- and n-type components by forming one continuous heterojunction. The efficiency of these architectures depends on the quality of the interface that is formed and the thickness of the individual components. In photovoltaics, for example, the use of layers that are too thin results in poor light absorption while layers that are too thick are subject to recombination losses. Alternatively, p-n heterojunctions with either multi-segmented or branched architectures will have a large number of interfaces available for electronic processes or chemical reactions to occur. Endeavors to develop optimal systems have resulted in the design of metal oxide-metal oxide (metal chalcogenides), metal oxide-organic, and metal–metal oxide heterojunctions with a variety of architectures, morphologies, and functionalities, as discussed:

4.1. Metal oxide-metal oxide (metal chalcogenides) p-n heterojunctions

Zinc oxide (ZnO) and titanium (IV) oxide (TiO_2) are two of the most frequently used semiconducting metal oxides for electronic applications. Although being heavily used in the semiconductor industry, their applicability can be hindered by their poor electrical conductivity and wide bandgaps (3–3.4 eV) which result in primary absorption of ultraviolet light and fast recombination. To overcome these limitations, semiconducting metal oxides are often paired with metal chalcogenides or other metal oxides (i.e., SnS, CdS, SnO_2, NiO) to form a heterojunction with enhanced optoelectronic properties. The interface quality is dependent on the level of lattice mismatch between the individual components, with lower degrees of mismatch being favorable. In addition to material selection, the synthesis method employed for fabricating heterojunctions also contributes to the amount of mismatch observed. As such, a variety of synthetic strategies have been developed for the formation of 1D all-inorganic p-n heterostructure with low lattice mismatch. In 2010, Zhang and coworkers reported the fabrication of a 1D NiO–ZnO heterostructure via electrospinning and calcination that showed improved photocatalytic activity in com-

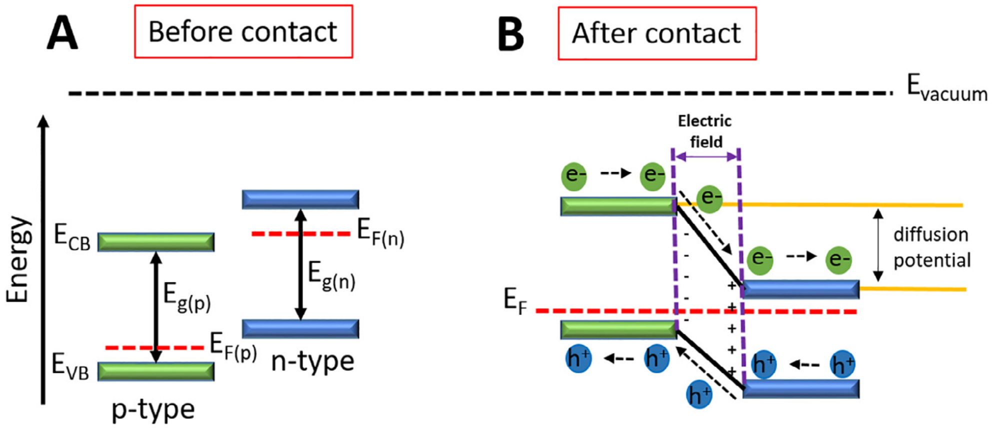

Fig. 4. Schematic representation of the energy level diagram for a p-n heterojunction. (A) p and n-type materials before contact and (B) formation of depletion region and electric field after contact.

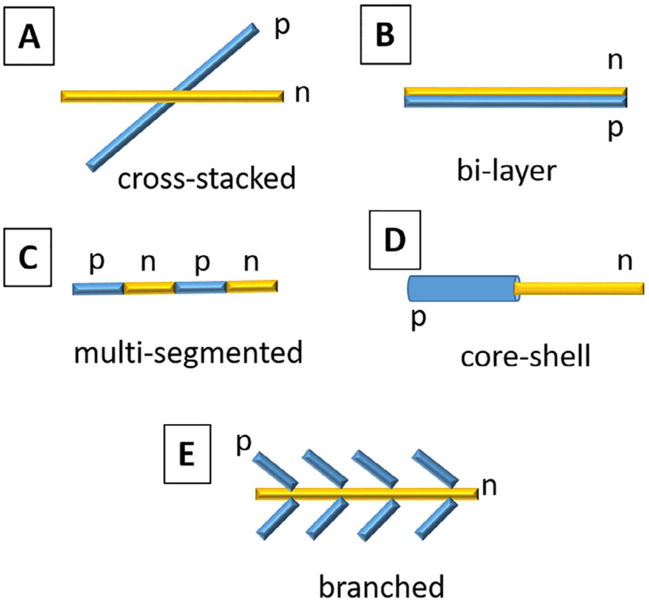

Fig. 5. Schematic representation of the various configurations that may yield a p-n heterojunction. (A) Cross-stacked, (B) bilayer, (C) multi-segmented, (D) core–shell, and (E) branched structure. Adapted *from J. Mater. Chem. C*, 2016, **4**, 9388–9398 with permission of The Royal Society of Chemistry [47].

parison to the individual components [46]. Nanofibers of varying molar ratios of NiO to ZnO were prepared from a single precursor solution of nickel acetate, zinc acetate, and polyacrylonitrile. The fibers maintained crystallinity consistent with NiO and ZnO. As shown in the high-resolution transmission electron microscope (HRTEM) images presented in Fig. 6, nanofibers composed of nanoparticles are formed through the electrospinning technique and a distinct interface of lattice fringes could be observed between the two materials, suggesting the formation of a heterostructure. Further analysis of the chemical environments of the NiO, ZnO and NiO–ZnO nanofibers indicate the presence of Ni-O-Zn bonds at the interface.

In addition to electrospinning, metal oxide-inorganic p-n heterostructures with low lattice mismatch have also been fabricated by CVD [48–50]. Wang and coworkers demonstrated the successful fabrication of a core–shell p-n heterojunction based on ZnO and the ternary alloy ZnS_xSe_{1-x} through a two-step deposition technique. In this work, ZnO was first grown at 1000 °C on an n-type Si (100) substrate using gold as the catalyst. Subsequently, the ZnS_xSe_{1-x} shell was deposited from a mixture of ZnS and ZnSe at 1100 °C to form the desired core–shell nanostructure [48]. As depicted in Fig. 7, the deposited ZnS_xSe_{1-x} layer is amorphous in nature while the ZnO core is crystalline as indicated by the selected-area electron diffraction (SAED) pattern and HRTEM images. The ZnS_xSe_{1-x} shell thickness may be controlled by adjusting the deposition time providing further tunability of the interaction between ZnO and ZnSe.

Hydrothermal/solvothermal syntheses have also been used to fabricate 1D metal oxide-metal oxide (metal chalcogenide) p-n heterostructures [51–53]. Peng et al. reported the two-step synthesis of Bi_2O_3-Bi_2WO_6 nanosheet-rod heterostructures where Bi_2O_3 and Bi_2WO_6 are used as p-type and n-type semiconductors, respectively. In their work, $Bi(OHC_2O_4)$ nanorods were synthesized from bismuth nitrate and sodium oxalate via hydrothermal synthesis at 120 °C and dried before being subjected to reaction with additional bismuth nitrate and sodium tungstate in a subsequent solvothermal reaction at 160 °C. Calcination of the Bi_2WO_6-$Bi(OHC_2O_4)$ composites in air afforded the desired heterostructure with varying ratios of Bi_2O_3 to Bi_2WO_6 with phase pure components as evidenced by structural and optoelectronic characterizations [52]. This 1D heterostructure displays a unique morphology, with nanoplatelets being stacked along a nanorod. Fig. 8A–D depicts the evolution in morphology corresponding to increasing amounts of n-Bi_2WO_6 nanoplatelets on the p-Bi_2O_3 nanowires. The relative positions of the conduction and valence band edges and the total densities for both components and the heterostructures can be further investigated via valence band XPS studies (Fig. 8E). Here, valence band onsets of 1.30 eV and 2.24 eV are observed for Bi_2O_3 and Bi_2WO_6, respectively, while the valence band for a heterostructure composed of a 2:3 ratio is at 1.70 eV. This shift in the energy of the valence band onset as well as the density of states near the Fermi level suggest the formation of a heterojunction between n-Bi_2WO_6 and p-Bi_2O_3.

4.2. Metal oxide-organic p-n heterojunctions

Metal oxide-organic p-n heterojunctions demonstrate great potential as they combine the best attributes of metal oxides (high electron mobility, high electron affinity, and physical stability) and organic (ease of processability, flexibility, and tunability via chemical modification) materials to afford new structures with unique functionalities. Electrostatic interactions enable the formation of p-n heterojunctions between electronegative organic and electropositive inorganic materials in self-assembled systems. Carboxylic acids, alcohols, amines, and thiols are commonly employed as functional groups that, upon deprotonation, bond

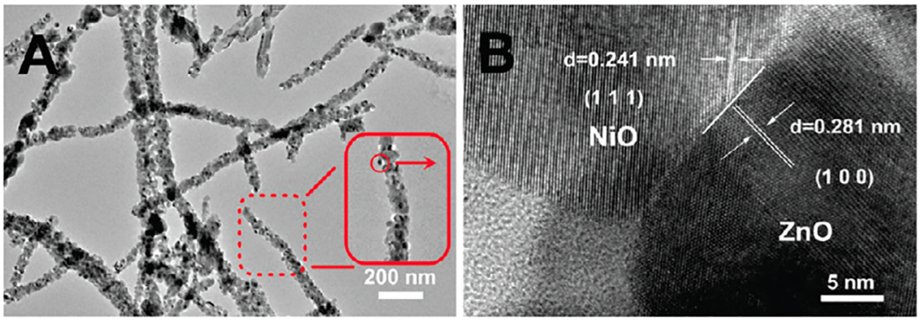

Fig. 6. (A) HRTEM image of as-electrospun NiO–ZnO nanofibers; (B) HRTEM of p-type NiO/n-type ZnO heterojunction region. Reprinted with permission from *ACS Appl. Mater. Interfaces* 2010, **2**, 2915–2923. Copyright (2010) American Chemical Society [46].

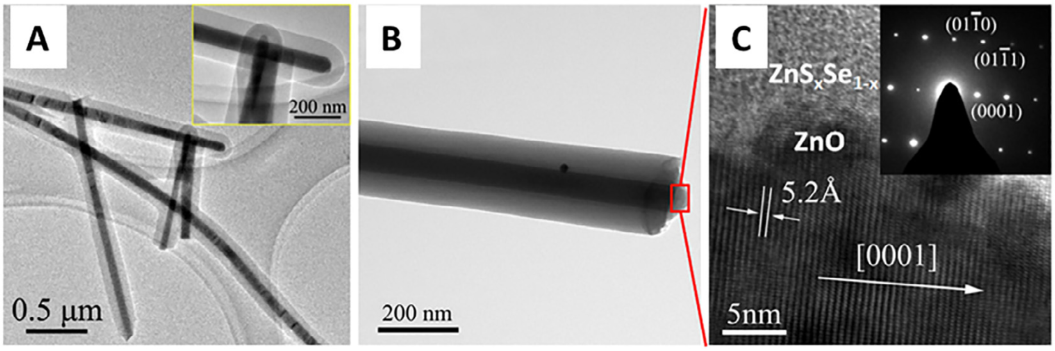

Fig. 7. (A) TEM image of ZnO–ZnS_xSe_{1-x} core–shell nanowires. Inset: TEM image for two nanowires where the core (ZnO) is surrounded by a shell (ZnS_xSe_{1-x}) structure. (B) Magnified TEM and (C) HRTEM images of a single ZnO–ZnS_xSe_{1-x} core–shell nanowire. Inset: SAED pattern of the core–shell nanowire. The diffraction peaks are associated only to crystalline ZnO. Adapted from *Appl. Phys. Lett.* **101**, 073105 with the permission of AIP Publishing [48].

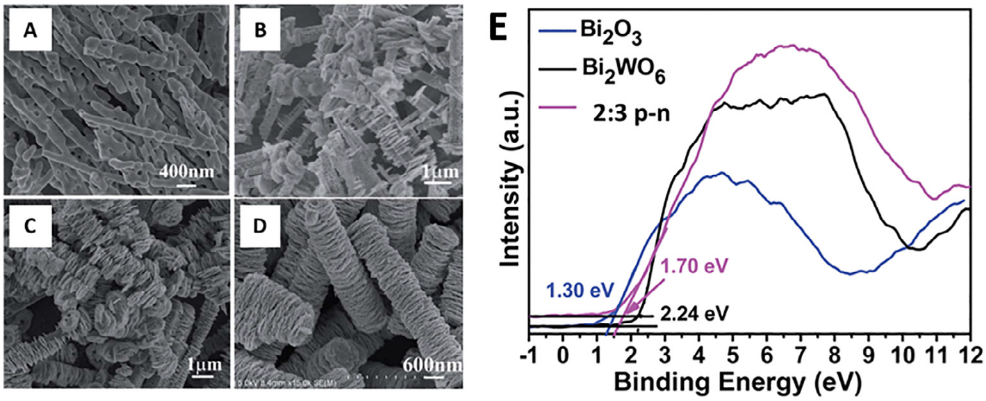

Fig. 8. SEM images of (A) pure Bi_2O_3, (B) 2:1.5 (mass) Bi_2O_3:Bi_2WO_6, (C) 2:3 (mass) Bi_2O_3:Bi_2WO_6, (D) 2:10 (mass) Bi_2O_3: Bi_2WO_6 (E) Valence band XPS spectra of Bi_2O_3, Bi_2WO_6 and 2:3 Bi_2O_3: Bi_2WO_6 samples. Adapted from *J. Mater. Chem. A*, 2014, **2**, 8517–8524 with permission of The Royal Society of Chemistry [52].

with positively charged metal oxides. Briseno et al. utilized these key interactions to chemically graft polymers such as poly(3-hexylthiophene-2,5-diyl (P3HT) and didodecyl quaterthiophene (QT) onto ZnO nanowires [54]. In their work, the organic components were functionalized with phosphonic esters to facilitate bonding between ZnO and P3HT and QT. Accordingly, chemical grafting was achieved by simply stirring a mixture of the organic and inorganic materials overnight. Fig. 9A-B depict the synthetic strategy while Fig. 9C-D depict the resulting core–shell structures. In addition to covalent bond formation between the nanowire and a phosphonic ester, hydrogen bonding and π–π interactions also occur between thiophene units to form shells greater than a monolayer in thickness. Thus, edge-on stacking of organic molecules governs shell thickness and can be controlled by varying the concentration of the solution containing the organic precursor. Work by Martini and coworkers demonstrated the importance of organic intermolecular interactions in determining outer shell thickness in heterojunctions comprising metal oxide nanostructures [55]. When the oligothiophene is modified using an asymmetric thiophene having a carboxylic acid as the ZnO binding site and unsubstituted alkyl chain, only a monolayer outer shell is obtained demonstrating the need to carefully understand the role of electrostatic interactions in the formation of organic–inorganic core–shell structures.

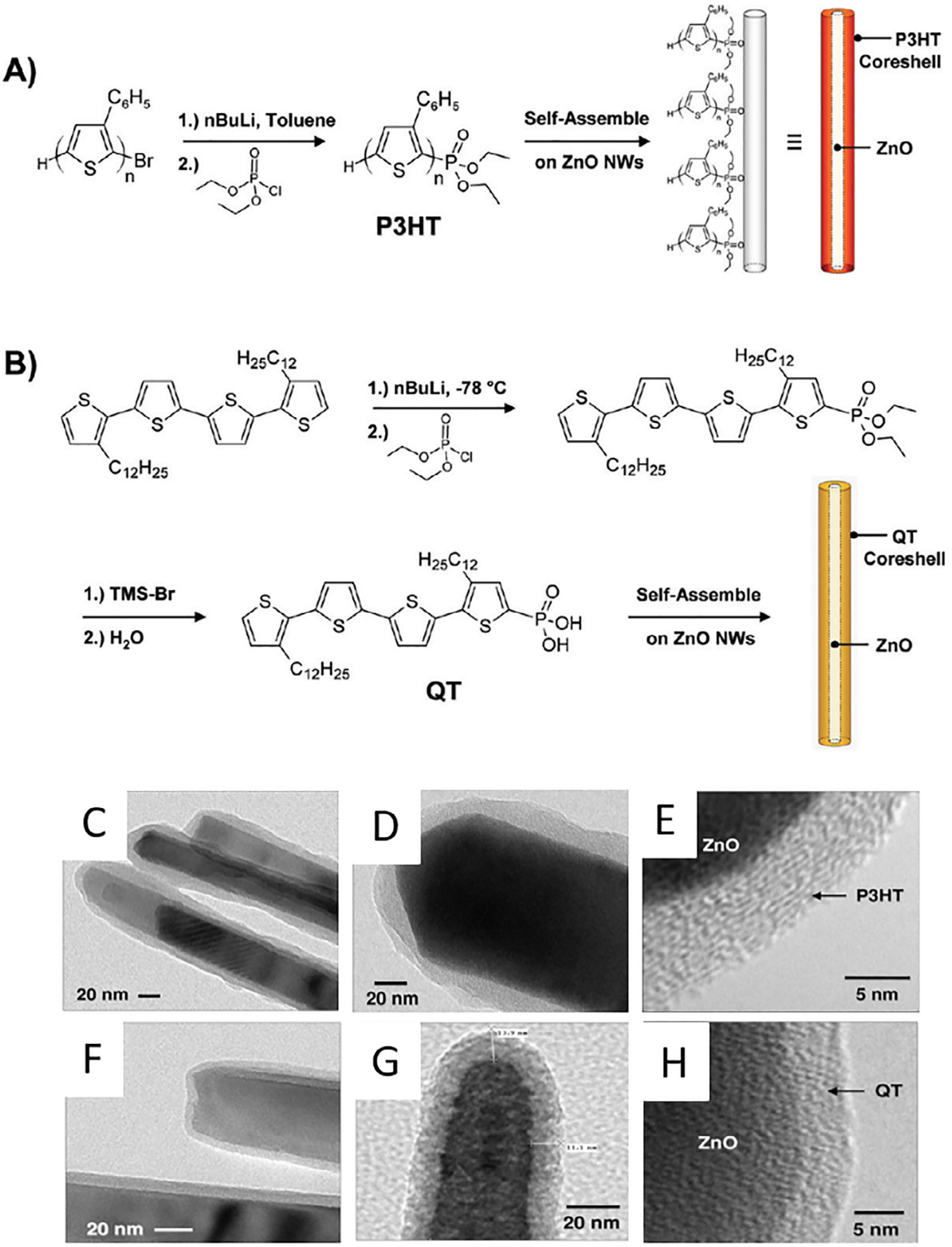

Fig. 9. Synthetic pathway for functionalizing a ZnO nanowire with (A) poly(3-hexylthiophene) (P3HT) and (B) didodecylquaterthiophene (QT) using a phosphonic ester and a phosphonic acid as anchors, respectively. TEM images of ZnO/P3HT core–shell nanowires (C–E) and ZnO/QT core–shell nanowires (F–H). Reprinted with permission from *Nano Lett.*, 2010, **10**, 334–340. Copyright (2010) American Chemical Society [54].

5. Metal oxides: electronic properties as a function of processing conditions

The chemical and physical nature of the metal–oxygen bonds may display different interactions that could yield metal oxides that are purely ionic or covalent. With the ability to control and manipulate these interactions under different processing conditions, metal oxides can exhibit a variety of electrical properties: they can behave as conductors, as well as insulators, and display electronic and magnetic properties that can vary with temperature, pressure, and composition [56].

As interest in characterizing metal oxides for applications including catalysis, electronics, and energy storage grows, two key molecular quantum parameters need to be taken into consideration to define key physical and chemical properties. The first parameter is electronegativity, χ, defined by Pauling as an atom's ability to attract electrons and quantified by Mulliken as the average between the absolute values of the ionization energy, *IE*, and of the electron affinity, *EA*. When referring to solids, the electronegativity coincides with the Fermi level (E_F). Likewise, the energy needed to remove an electron at the Fermi level from the surface of a solid (WF) is also related to E_F (WF = $E_{vac} - E_F$) as shown in

Fig. 10 [57]. All semiconductors and insulators have an energy gap (E_g) also known as a transport gap which is the energy needed to excite an electron from the valence band (VB) into the conduction band (CB). The E_g value as well as the energy positions of both the VB and CB are of paramount importance when identifying carrier injection and extraction barrier pathways at metal/metal oxide, organic/metal oxide, and metal oxide/metal oxide interfaces.

The second parameter is chemical hardness, η, which Parr and Pearson defined as one half of the difference between the ionization potential and the electron affinity [58]. Conceptually, chemical hardness is better known in terms of acid–base interactions. Hard acids prefer binding to hard bases, and soft acids prefer binding to soft bases. In this context, "hard" refers to small, non-polarizable, highly-charged species, and the term "soft," to larger, more polarizable, less charged reagents [59]. Previous studies have concluded that high χ and strong η are characteristic of acidic oxides whereas low χ and weak η tend to describe basic metal oxides (Table 1) [60].

5.1. Electronic properties

Carrier mobility is one important parameter to consider when tuning the electrical properties of metal oxides. This can be tuned by modifications in their pre- and post-processing procedures. Increasing the carrier mobility parameter of the semiconductors comprising the different layers in a device can have favorable effects on its overall performance. For example, increasing carrier mobility in a material may affect the source-drain current in a field-effect transistor as well as the ability for efficient charge transport to electrodes in solar cells [2]. The enhanced mobility of metal oxides compared to that of a-Si is largely due to differences in their electronic structure. In early transition metal oxides, such as TiO_2, the valence band maximum (VBM) is mainly comprised of O 2p antibonding states, while the conduction band minimum (CBM) is comprised mainly of empty metal d states [2,61,62]. This is demonstrated in the calculated total TiO_2 and projected Ti 3d and O 2p density of states presented in Fig. 11 [61,63]. In late transition metal oxides, such as indium- gallium-zinc oxide (IGZO), completely filled d-orbitals allow for the main contribution to the CBM to be from unoccupied ns metal bonding states (Fig. 12) [64]. Due to their spherical shape, the metal ns orbitals are able to remain energetically overlapped and retain good electron mobility, even if the crystal structure is disordered, as in polycrystalline and amorphous metal oxides (Fig. 12A). This provides a major advantage over silicon, where sp^3 hybridization does not permit the retention of good electron mobility when the lattice is distorted (Fig. 12B) [2,62,65,66]. While the molecular orbital hybridization has a major effect on the mobility of metal oxides, carrier mobility can be greatly affected by processing conditions during and after deposition.

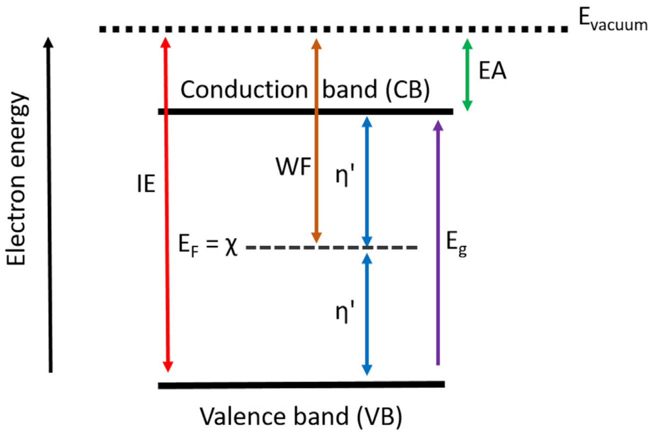

Fig. 10. Schematic depiction of the energy level diagram for an undoped semiconductor with flat bands to the surface highlighting the position of the bandgap (E_g), Fermi level (E_F), ionization energy (IE), electron affinity (EA), work function (WF), and chemical hardness (η).

Table 1
Chemical hardness and electronegativity trends for metal oxides.

	Strong electronegativity	Weak electronegativity
Strong chemical hardness	Insulators with a large optical bandgap (e.g., B_2O_3, BeO, Al_2O_3)	Ionic oxides with a relatively large optical bandgap (e.g., ZnO, SnO_2, Bi_2O_3)
Weak chemical hardness	Oxides of transition elements with high oxidation state (e.g., TiO_2, WO_3, V_2O_5)	Alkali and alkaline earth oxides (e.g., K_2O, Cs_2O, MgO)

Common deposition methods used in the fabrication of metal oxides include vapor processing (thermal evaporation, atomic layer deposition (ALD), sputtering, and pulsed laser deposition), sol–gel chemistry (spin- or dip-coating), printing (ink-jet, aerosol-jet, gravure, and roll-to-roll), and combustion (spin or spray). Factors within each process can be varied, such as time, temperature, pressure, thickness, deposition rate and the addition of gases. Common post-processing techniques include thermal annealing at high or low temperatures, encapsulation, plasma treatment, and UV light exposure. These fabrication methods, as well as variations in post-processing conditions, can have significant effects on the electron mobility of metal oxides. Table 2 compares the electron mobility (µe) values for ZnO processed by vapor deposition [64,67] sol–gel [68,69], printing [70], and spray pyrolysis [71]. As shown, it is evident that certain processing techniques produce much higher µe values than others. Through vapor deposition, a µe as high as 20.2 $cm^2\ V^{-1}\ s^{-1}$ may be obtained, while ZnO structures fabricated by other deposition techniques have mobility values <10 $cm^2\ V^{-1}\ s^{-1}$. Vapor-assisted deposition processes typically yield the best film quality (i.e., few pinholes, few grain boundaries, large crystal grains), since they offer more control over the film morphology and fine tuning of the crystal structure by adjustments of the target composition or various gas partial pressures during deposition. Although effective, vapor-processing techniques are expensive and require specialized equipment, so other more practical techniques are often utilized. Even within a processing category, there is variation. For instance, when ZnO is deposited via atomic layer deposition (ALD) it achieves its highest µe (20.2 cm^2 -$V^{-1}\ s^{-1}$) but when sputter deposition is utilized; µe is a low 1.2 $cm^2\ V^{-1}\ s^{-1}$ (Table 2). This discrepancy in µe may be attributed to other factors that can be modified during deposition, such as defect concentration and oxygen vacancies, but may also be due to post-processing annealing temperatures. As evidenced in Table 2, increasing annealing temperatures may increase µe. However for many applications, like organic or flexible electronics, low processing temperatures are required to prevent degradation of the other components of the device. Fig. 13 displays the relationship between annealing temperature and µe for commonly used metal oxides, such as indium oxide (In_2O_3), zinc tin oxide (ZTO), and indium zinc oxide (IZO). The µe for the crystalline structures (red circle) is much higher than that of the amorphous structures (blue square) at all temperatures. This is due to better alignment of the molecular orbitals as discussed earlier. For all of the metal oxides shown in Fig. 13, µe is increased exponentially as the temperature is increased [1]. High temperatures may be a product of the deposition technique (thermal evaporation) or they may be required to induce crystallinity, adhesion to the substrate, or remove the excess solvent (sol–gel). One of the goals in the semiconductor industry concerning metal oxide processing is to achieve

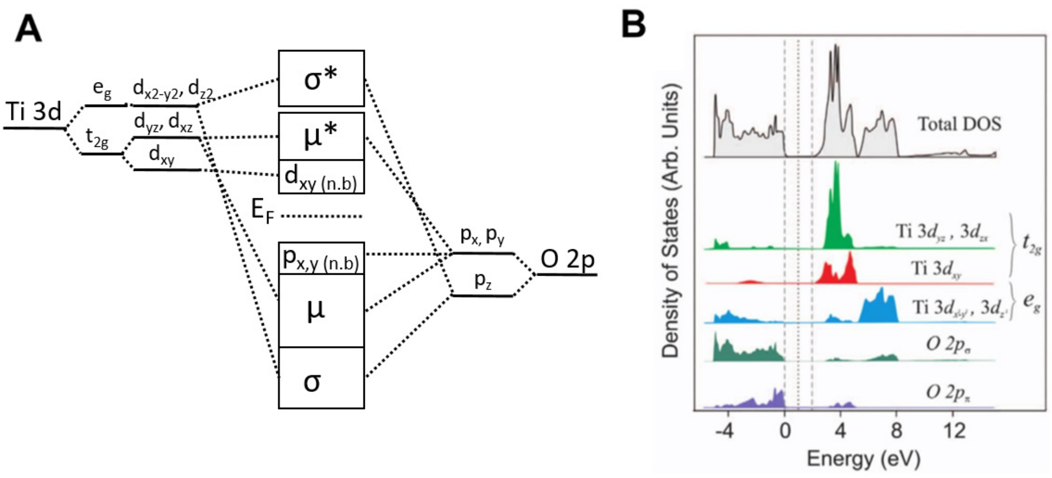

Fig. 11. (A) Molecular orbital energy level diagram for anatase TiO_2. (B) Calculated total (top) and projected density of states (below) for Ti 3*d* and O 2*p* orbitals. Adapted from *Acta Crystallogr. Sect. A Found. Crystallogr.* **2003**, *59*, 341–350 with permission of the International Union of Crystallography [63].

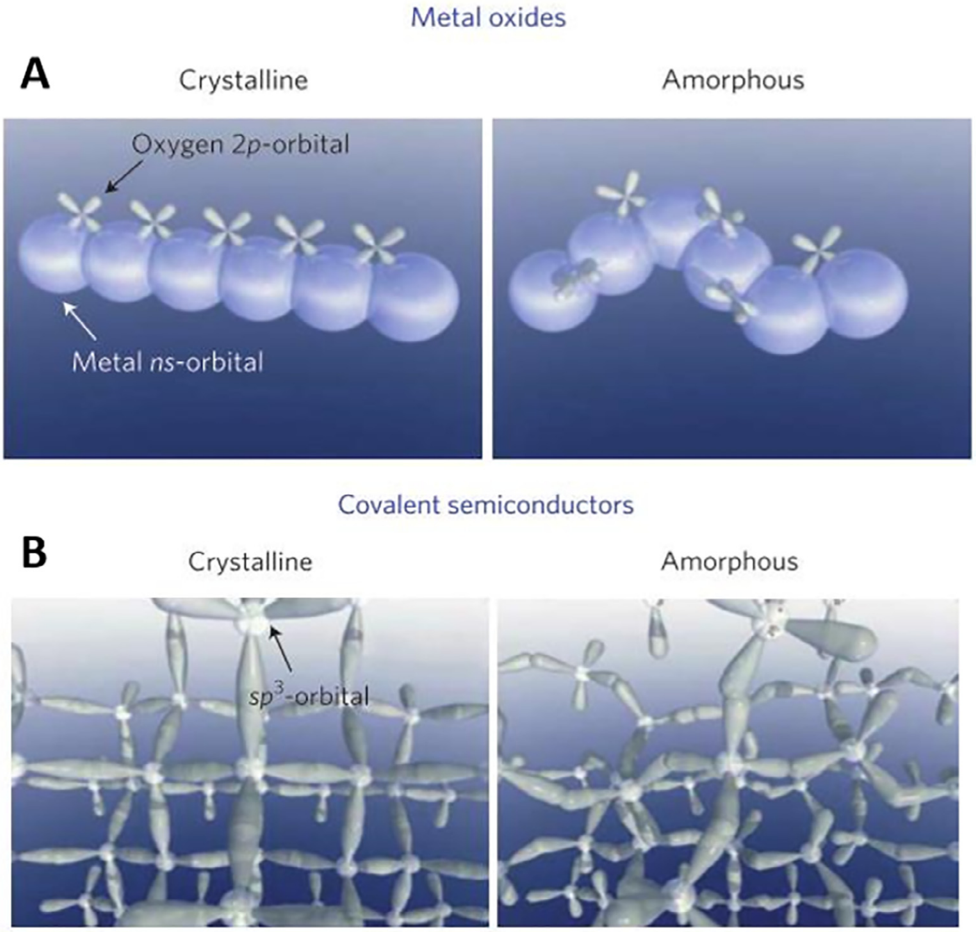

Fig. 12. Representation of the atomic orbital hybridization in crystalline (left) and amorphous (right) metal oxide (A) and silicon (B). Reprinted by permission from Springer Nature Publishing AG: *Nature* **2004**, *432*, 488–492. Copyright 2003 [64].

the highest μe associated with high temperature or vapor processing, but with inexpensive, low-temperature fabrication methods. To achieve this, the processing conditions of the metal oxide must be optimized, and the chemistry particularly related to defects formation must be understood.

5.2. Defects in metal oxides

As a product of nature, no crystal lattice is perfect. Metal oxides are prone to four major types of defects in their lattices: oxygen (O) or metal (M) vacancies, M or O interstitials, O on an M site, or M on

Table 2
Effect of processing conditions on the μe of ZnO.

Fabrication process	μe ($cm^2 V^{-1} s^{-1}$)	Annealing temperature (°C)	References
Vapor deposition	20.2 (ALD)	90	[64]
	1.2 (sputtering)	25	[67]
Sol–gel	10.0	180	[68]
	5.3	500	[69]
Printing	1.6	250	[70]
Spray pyrolysis	15.0	400	[71]
	0.1	200	[71]

an O site. Defects can affect many properties of metal oxides that are important for device function including mobility, trap density, and energy level alignment. The formation energies of these defects are different for each metal oxide, and therefore two metal oxides at the same temperature may contain different defect concentrations. Further, for a certain metal oxide, the formation energies of the various defects are typically different. This gives rise to intrinsically n- or p-doped metal oxides. Since O vacancies are the most common type of defect in metal oxides, we will focus on how they affect metal oxides particularly when used in photovoltaic and electronic applications [61].

When an O vacancy forms, it leaves behind an under-coordinated metal center having an extra electron. This extra electron will occupy an empty metal d-band states close to the CBM, acting as an n-type dopant. Fig. 14 displays the filling of metal d-states when oxygen vacancies are formed in a metal oxide. A pristine metal oxide with no defects is schematically represented in Fig. 14A. Here, the Fermi level is set to 0 eV and filled orbitals are represented by a finite density of states at positive binding energies. The VBM is comprised mostly of oxygen 2p states (3–4 eV), and there are no mid-gap states occupied in the 0–3 eV region, leaving the metal d-states (near the Fermi level) empty. When O vacancies arise, empty metal d-states are filled. This is displayed in Fig. 14B, where a finite density of states arises in the 1–2 eV region. Since these newly occupied states are close in energy to the CBM, they act as n-type dopants [72]. This is the case for TiO_2, the most commonly used electron transporting layer in hybrid organic–inorganic photovoltaics, which will be discussed later.

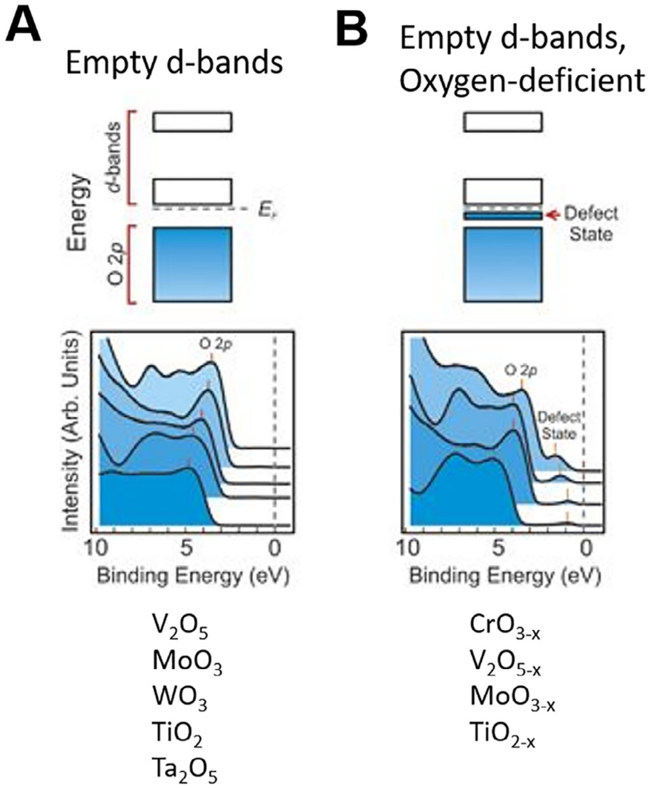

Fig. 14. Schematic energy band diagrams (top) and ultraviolet photoelectron spectra of (A) pristine and (B) oxygen-deficient metal oxides. Reprinted by permission from Springer Nature Publishing AG: *Nat. Mater.*, **2011**, 11, 76–81. Copyright 2011.[72]

As O vacancies leave behind excess charges, they can increase the carrier concentration of the metal oxide. The conductivity of a metal oxide film is dependent on the mobility and the carrier concentration, so increasing the carrier concentration via adding O vacancies will increase the conductivity. In addition to conductivity enhancement, O vacancies can modify the work function of a metal oxide and could modify the energy level alignment of the different materials and interfaces within an electronic device. When an extra electron is left on a metal center, its oxidation state is decreased, and its electronegativity (mid-point between ionization energy and electron affinity) is decreased. Since the Fermi level of an undoped metal oxide is also at the mid-gap, the Fermi level and electronegativity are directly related [60,73]. The ability to tune the Fermi level, and therefore the WF, of a metal oxide

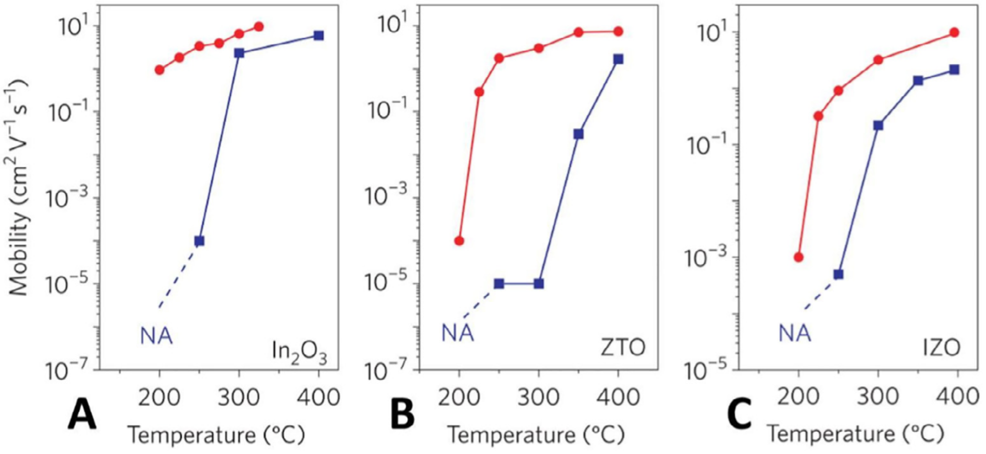

Fig. 13. Measured changes in mobility as a function of temperature for crystalline (red) and amorphous (blue) (A) indium oxide (In_2O_3) (B) zinc tin oxide (ZTO) (C) indium zinc oxide (IZO). Reprinted by permission from Springer Nature Publishing AG: *Nat. Mater.* **2011**, 10, 382–388. Copyright 2011 [1]. (Colour online.)

has been displayed most prominently in molybdenum oxide (MoO_3) (Fig. 15) [74]. The energy level diagram in Fig. 15A shows the defect states occupied in MoO_3 due to O vacancies. As the concentration of these defect states increases, a reduction in WF is shown as the secondary electron cutoff energy is increased (blue to purple). The decrease in WF is also correlated to an increase in the occupancy of defect states above the VBM (Fig. 15B-D). The change in WF of MoO_{3-x} as a function of O defects (x) is displayed in Fig. 15E, where a change in WF of over 0.5 eV is observed from MoO_3 to MoO_2 [74]. While other factors, such as surface roughness, exposed crystal facet, impurities and post-processing treatments, can affect the WF of a material, the ability to control the concentration of O vacancies may offer further control over the electronic structure of metal oxides as a means to target a specific function.

However, not everything is sunshine and rainbows as O vacancies may also be detrimental to metal oxides. The greatest disadvantage that O vacancies can have is forming trap states themselves. Depending on the energy position of the leftover electron, it can be in an optimal position to recombine with a hole. When this type of trap-assisted recombination occurs in optoelectronic devices, it prevents charge transfer to the electrodes, and reduces the overall efficiency of the device. Since defects, particularly O vacancies, can affect the electronic structure of metal oxides, research efforts have been focused on finding fabrication pathways to control their concentration mainly in thin film metal oxides. In vapor deposition, the partial pressure of O_2 can be controlled. By maintaining a high or low partial pressure of O_2 during deposition, selectivity for a low or high concentration of defects, respectively, can be achieved. Certain processing conditions themselves can be prone to more or fewer defects as well. For example, sol–gel processing is performed in a less-controlled environment, which makes it much less expensive; however, because of this, the opportunity for defect formation is higher. Normally sol–gel processing yields amorphous metal oxides. High-temperature annealing is a great way to induce crystallinity and in turn, it reduces defects due to the elimination of O vacancies and residual precursors [62]. Other post-processing treatments have proven effective at controlling defect concentration. The addition of a In_2O_3 thin film as a capping layer is effective in preventing O out-diffusion from metal oxide films, which eliminates changes in the concentration of O vacancy defects over time [75]. In metal oxide nanoparticles, ligand passivation can be an effective mean of filling surface traps [76]. Surface passivation using small molecules and self-assembled monolayers has been very effective for passivating surface defects as well [77–81]. UV-irradiation has also been explored as a post-processing technique. This has been found to induce crystallinity and condensation of sol–gel deposited metal oxide films [82]. In addition, UV light promotes the formation of O radicals that eliminate impurities within the crystal thus, reducing traps created by residual precursors [82]. Doping of metal oxides has not only been effective at enhancing electron mobility (Li^+, Nb^{4+}, Zn^{2+}, Y^{3+}, Zr^{4+}, and Mo^{4+}) but also for filling O vacancies [83–85]. Using a fluorine plasma treatment, O vacancies in ZnO could be filled with F, and the defect concentration could be reduced, leading to more efficient devices [86]. Understanding the chemistry behind the active role that defects, specifically O vacancies, has on the properties of semiconductor metal oxides is of vital importance to modern electronics.

On the contrary, we have yet to discuss the design and use of metal oxides as p-type materials for energy conversion. It is known that metal oxides having a high density of metal vacancies will exhibit p-type behavior [87]. However, too many metal vacancies will lead to surface-mediated recombination which detrimentally affects electrical conductivity and mobility. Given the challenge faced in controlling metal vacancies when compared to oxygen vacancies, most materials engineering efforts have lagged behind in the development of high efficient p-type metal oxides. The challenge stems from the inability to control the localized O 2p dominated valence band and high density of deep traps near the valence band where holes are trapped by O ions [1,2]. As such, the formation of p-type metal oxides may be achieved by engineering their band structure and band energy as well as tuning their crystal structure. For example, p-type NiO_x with high electrical conductivity and mobility may be prepared by increasing the density of Ni^{3+} ions upon the addition of a monovalent atom such as lithium or by the appearance of nickel vacancies and/or interstitial oxygen in NiO_x crystallites [88–90]. NiO in particular is well-known to have a high density of nickel vacancies that results in p-type doping [91]. Therefore, the most common p-type metal oxide is NiO_x but other binary oxides such as CuO_x, MoO_3, V_2O_5, or GeO_2 are also under investigation. In order to improve the performance of these p-type metal oxides, so they are comparable to their n-type counterparts, approaches are currently being developed to enhance valence band dispersion to reduce effective mass and increase mobility [92]. Additionally the crystal structure of these metal oxides must also be considered because it determines the coordination and the spatial stacking of the cation and anions [92]. For example, a tetrahedrally coordinated system is beneficial because all eight electrons of the oxygen participate in the four sigma bonds which allows for further delocalization of the valence band

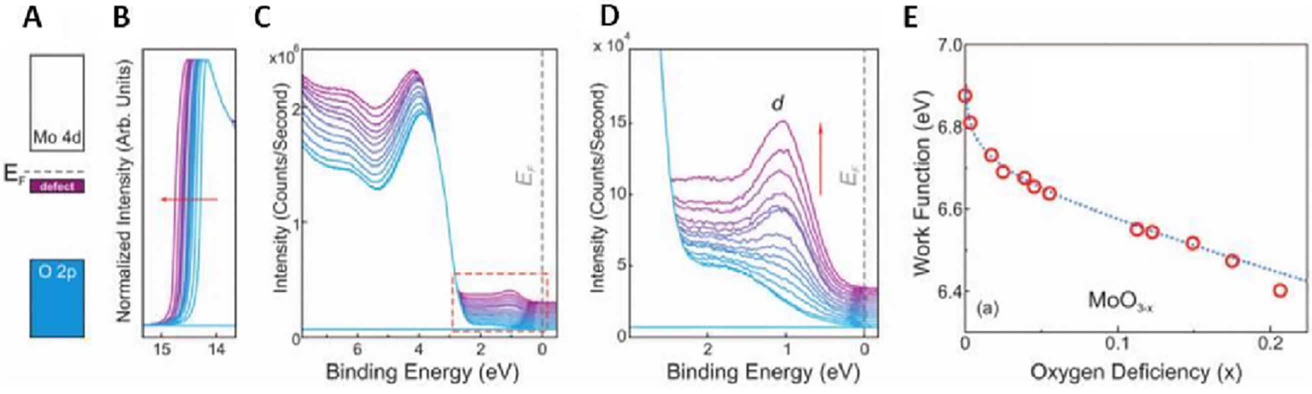

Fig. 15. UPS analysis of O-deficient MoO_3. (A) Schematic energy level diagram of MoO_3 with oxygen defects (Fermi level (E_F), O 2p band, Mo 4d band, and defect band are indicated for clarity). (B) UPS spectra of the high binding energy region of MoO_3 showing an increase in the secondary electron cutoff as defects are added. (C, D) UPS spectra of the low binding energy region of the MoO_3 spectra, showing the growth of occupied defect states above the VBM. (E) Work function for MoO_3 vs. oxygen deficiency. Reprinted by permission from John Wiley & Sons, Inc: John Wiley and Sons, *Adv. Funct. Mater.* **2012**, *22*, 4557–4568. Copyright 2012 [74].

edge. Using the insights gained from changes in the energy level alignment, crystallinity, and defect concentrations of metal oxides as a function of processing conditions allow us to form structure–function relationships toward the design of efficient devices.

6. Applications involving the use of metal oxides

The morphological variety of metal oxides is incomparable, whether, in the form of nanoparticles, nanowires, smooth thin films, or mesoporous layers, they can be relatively easily adapted to accommodate a huge variety of device needs and applications. Thus the questions to ask are, what makes metal oxides so unique? -this will prompt us to formulate a second question, what would metal oxides do? (WWMOD). To answer these questions, we need to think of metal oxides as ionic solids composed of positive metallic species and oxygen ions with strong ionicity. Electronically, metal oxides have a filled s shell, however, their d shells are empty or partially filled giving a large degree of freedom for tuning their optical and electronic properties. For example, it is possible to achieve metal oxides with narrow bandgaps (e.g., Mn_2O_3, E_g = 0.5 -eV; CuO, E_g = 1.3 eV) [93,94] wide bandgaps (e.g., SnO_2, E_g = 3.8 eV; TiO_2, E_g = 3.3; ZnO, E_g = 3.4 eV) [95–98] as well as ultrawide bandgaps (e.g., Al_2O_3, E_g = 7.0 eV; Ga_2O_3, E_g = 4.5 eV) depending on how their orbitals are filled [99,100]. Similarly, it is possible to achieve metal oxides with tunable dielectric constants [101–103], and superb electrical [104], optical [105], and electrochromic properties [106]. Thus, given the ability to tailor the physical and chemical properties of metal oxides, they have been incorporated as functional materials in a wide range of technologies such as batteries [107–112], catalysis [113–116], smart window coatings [117–123], photovoltaics [96,124–128], photoelectrochemical cells [129–135], fuel cells [136–139], plasmonic smart windows [140,141], contrast agents for magnetic resonance imaging [142–144], and biodegradation of organic pollutants [145–147]. Due to the large breath of applications that have benefited from incorporating metal oxides in their device stack, we will proceed to narrow the focus of the following section to only discuss the use of metal oxides for energy related applications i.e., photovoltaics, plasmonics, and Braggs reflectors. The latter is a nice addition to this review as previous perspectives on metal oxides have hardly ever covered this particular application.

6.1. All inorganic photovoltaics

The continuous success of Si solar cells, but at high costs, leads to interest in incorporating other materials that are cheaper and more accessible. The alternative materials could complement or eventually replace Si without compromising power conversion efficiencies. A p-type c-Si wafer with a front phosphorous diffusion and a full-area aluminum (Al) alloyed rear surface region is the common architecture for these solar cells. The Al layer is associated with a high contact resistance even with the small difference between the work function of Al and Si. The resulting contact resistance is induced by a high density of bandgap states or defects at the metal/semiconductor interface leading to a relatively high Schottky barrier height of approximately 0.65 eV [148]. A large barrier height is detrimental to the flow of electrons out of the n-type Si wafers. This issue inspired the exploration of the dependence of contact resistivity. There have been many different approaches to reduce the contact resistivity, one straightforward method involves reducing the Schottky barrier height. One technique for this would require depinning the Fermi level by inserting an interfacial layer between the metal/semiconductor interface [148,149]. The interlayer must function as a passivating layer that can reduce the density of states/defects while still being conductive enough to allow sufficient charge transport. Materials for electron-selective contacts on n-type c-Si with these properties have been explored and metal oxides such as MgO have been reported to improve the Ohmic contact significantly, thus increasing fill factors and power conversion efficiencies due to the materials ability to reduce recombination loses [148,150]. In addition to using metal oxides as electron selective and passivating interfacial layers, other oxides have been utilized as hole selective (p-type) contacts in inorganic photovoltaics. Transition metal oxides such as MoO_3, NiO, WO_3, and V_2O_5, have all been investigated as p-type contacts for n-type crystalline silicon heterojunction photovoltaics [151–157]. These oxides make appropriate transparent hole-selective contacts in a solar cell due to their high work functions and wide energy bandgaps. These properties are due to metal site defects present in their lattice [151].

Conversely, metal oxides can also be used as solar absorbers in all inorganic solar cells (not containing silicon). As such, the influence of the electronic properties at these metal oxide thin-film heterojunction interfaces is critical for device performance. Focusing on sputter-deposited Cu_2O thin films as the absorber layer in an Al-doped ZnO/Cu_2O inorganic solar cell, it is necessary to create a heterojunction with a relatively low conduction band offset. Many manipulations can be done to aid in the energy band alignment including adjusting the deposition conditions, post-deposition treatment of the Cu_2O layer, or incorporating a buffer layer. Nordseth et al. used the control of the magnetron sputtering technique and post-thermal annealing process to manipulate the deposition conditions to control the electronic properties at the heterojunction interface [158–160]. With this control, suitable energy band alignment at the interface as well as the ability to improve the electrical characteristics of the heterostructure are possible. In the Al-doped ZnO/Cu_2O heterojunction inorganic photovoltaic, a thin buffer layer of 10 nm is incorporated between the two oxides due to the formation of an even thinner interface defect layer forming atop the Cu_2O surface. This defect layer is known to be an intermediate CuO layer, formed due to the small enthalpy of formation for Cu_2O which makes the interface prone to oxidation. The defect density is especially high at this interface layer and creates issues for energy band alignment, which is why the buffer layer is so crucial in this device architecture. The buffer layer itself is $Zn_{1-x}Ge_xO$, but other metal oxides, such as Ga_2O_3 and TiO_2 have also been used as buffer layers. These buffer materials not only aid in the modulation of the conduction band offset but also works to improve the carrier collection as a result of suppressed interface recombination [160,161].

6.2. Organic photovoltaics

Indium-doped tin oxide (ITO) is the most commonly used electrode in organic solar cells. The work function of ITO allows it to be used as the hole-extracting layer in conventional organic photovoltaics whereas, it is used as an electron-extracting layer in inverted photovoltaics. Fluorine-doped tin oxide (FTO) is also a popular transparent conducting oxide used as an electrode in photovoltaics. This is due to its thermal stability in devices that require higher temperature processing or potentially better energy level alignment [162]. Another commonly used oxide in organic solar cells is molybdenum oxide (MoO_x). This material works as an interfacial layer between the photoactive layer and anode playing a crucial role in enhancing the power conversion efficiencies of organic photovoltaics by facilitating hole extraction and transport [163–165]. Besides being a good hole extraction material, MoO_x is also pH neutral, non-toxic, environmentally stable, and transparent in the visible [164,166].

In an inverted organic solar cell architecture, a metal oxide, commonly ZnO or TiO_2, is layered on the ITO electrode as an electron-transporting layer. This additional oxide layer then inverts the polarity of the bulk heterojunction device and will yield higher power conversion efficiencies than those without the layer [167–169]. The main disadvantage of using these metal oxide layers is that the sol–gel method used in the fabrication requires high temperatures to induce crystallinity; thus, limiting substrate flexibility. The high-temperature sol–gel fabrication method could also lead to non-stoichiometric metal oxides stemming from the evolution of oxygen vacancies and zinc interstitials [170,171]. These can introduce near-surface defects with adsorbed oxygen with poor morphology control. These defects could also detrimentally affect the adjacent organic layers and in turn decrease device efficiencies. Due to the increased stability of inverted organic solar cells as opposed to conventional solar cells, there is an extensive amount of research undertaken to either use low temperature fabrication methods that will lead to stoichiometric metal oxide thin films or to find metal oxide modification protocols allowing the tuning of surface energetics, energy levels, and passivation of defects.

The integration of highly-ordered, anisotropic, nanostructured semiconducting metal oxides within an organic bulk-heterojunction represents a vital goal for the development of next-generation photovoltaics. Such integration is imperative for improvements in photocurrent generation and light-harvesting efficiencies. To realize the full potential of metal oxide-organic hybrid photovoltaics, however, a number of formidable challenges need to be addressed, including the ability to control the assembly of organic and inorganic components; the ability to tune organic–inorganic interfaces, and the ability to guide the direction of charge transfer. Whittaker-Brooks et al. tackled a slice of this problem by engineering nanostructured inorganic semiconducting materials with tunable dimensions, morphologies, and photochemical properties to be assembled with organic semiconductors in hybrid solar cells. Critical to the controlled growth of inorganic semiconductor nanowire arrays is the deposition of a sputtered seed layer. For example, when oxidized, sputtered ZnO thin films are more homogeneous than their sol–gel derived ZnO thin film counterpart, thus creating more uniform nucleation sites for the growth of ZnO nanowires [80]. This sputtered seed layer also promotes the subsequent hydrothermal growth of vertically-oriented, one-dimensional ZnO nanostructures onto which poly-(3-hexylthiophene), P3HT, is subsequently deposited to complete the photoactive layer of the hybrid solar cell (Fig. 16A–C). With this seed layer, the external quantum efficiencies and photovoltaic conversion efficiencies of a hybrid solar cell are increased from 0.5% to 1.8%. (Fig. 16D) [97].

Depending on energy level misalignment, a significant barrier to charge injection may exist at interfaces between inorganic metals and metal oxides with organic semiconductors. The adsorption of self-assembled monolayers (SAM) onto inorganic metals and metal oxides represents a promising route to control their electronic characteristics and surface wettability with organic semiconductors. To achieve optimal functionality and stability at the interface, a structurally well-defined, and covalently bonded monolayer is needed. Amongst metal oxides, ZnO is widely used in many technological applications, such as organic light-emitting diodes and solar cells because of its high electron mobility and efficient electron transporting properties. Yet, ZnO-organic photovoltaics have shown disappointingly poor performance, likely because of surface defects. Surface functionalization of ZnO with SAM before the deposition of the organic semiconductor thus represents an interesting approach that provides access to tunable chemical and physical properties of the inorganic–organic interface. In a follow-up publication, Whittaker-Brooks et al. reported a stepwise functionalization method that allows binding of small acidic molecules to ZnO nanowire arrays with minimal surface degradation and etching. Given their high acidity, adsorption via dip-coating and spin-coating organophosphonic acid solutions on

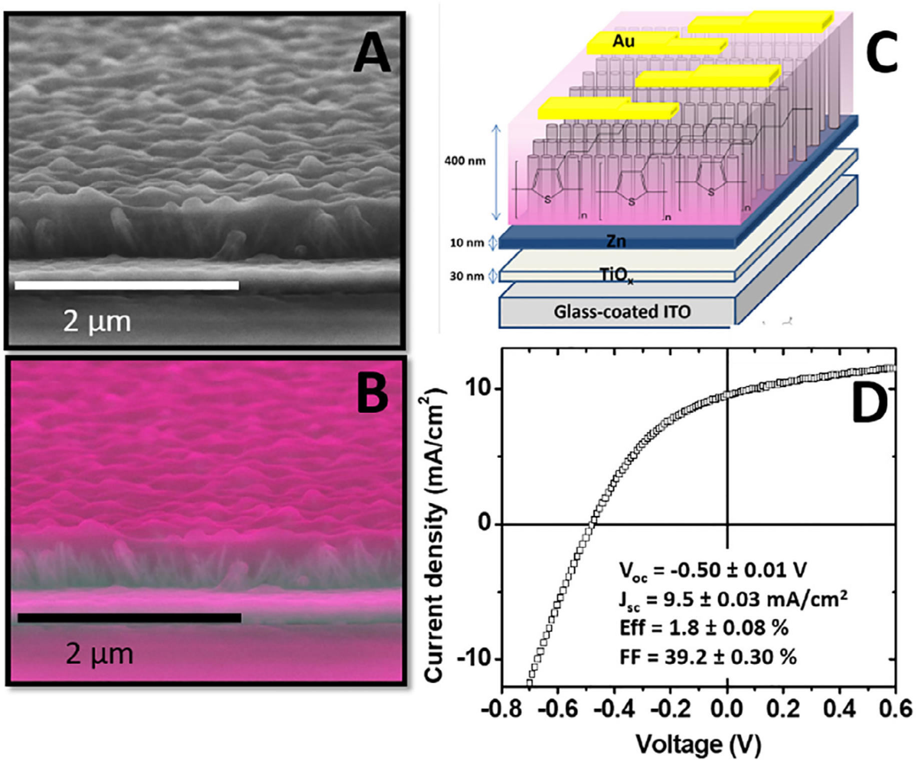

Fig. 16. (A) Cross-sectional SEM image of P3HT infiltrated into ZnO nanowire arrays. (B) Colored backscattering SEM image showing the filling of the polymer donor into the ZnO nanowire array. (C) Device architecture used for the fabrication of ZnO-P3HT inverted solar cells. (D) J–V characteristics for a representative ZnO nanowire:P3HT bulk-heterojunction solar cell whose ZnO nanowires were grown from a sputtered seed layer.

ZnO nanowire arrays uniformly degrade the structures. They also reported that SAM adsorption via tethering-by-aggregation-and-growth (T-BAG) yield robust surface-bound monolayers on ZnO nanowire arrays while retaining the nanostructure morphology. These phosphonic acid-functionalized ZnO nanowires were incorporated in hybrid organic–inorganic solar cells with infiltrated P3HT, as the organic donor. Inverted solar cell devices fabricated with these treated interfaces exhibit power conversion efficiencies as high as 2.3% due to improvements in both the short-circuit current density and the open-circuit voltage compared with analogous devices with untreated ZnO nanowire arrays that exhibit efficiencies of 1.8% (Fig. 17). They attributed the enhancement in device characteristics to improved charge transfer between P3HT and ZnO and reduced recombination at the organic–inorganic interface due to enhanced wettability between the constituents with SAM treatment. SAM adsorption also induces an interfacial dipole which modifies ZnO work function allowing for better energy level alignment with P3HT. Further, statistical and surface analyses have demonstrated that successful adsorption of phosphonic acid derivatives on the ZnO surfaces contributes to the passivation of interfacial traps [80].

Research performed on incorporating metal oxides into organic photovoltaics has created a better understanding of the fundamentals of device operation, including charge-separation processes, charge-transport mechanisms, device physics, and interfacial effects. This has led to the design of more efficient, stable device architectures based on materials with improved energy-level alignment, spectral response, and transport properties. Much of the research progress attained in organic photovoltaics can also transfer over to increase the efficiency and stability of organic–inorganic hybrid perovskite photovoltaics.

6.3. Organic-inorganic hybrid perovskite solar cells

Now we turn our attention to organic–inorganic hybrid perovskite solar cells (specifically photovoltaic cells using methylammonium lead iodide as the absorber) as metal oxides are incorporated in the device stack as either the electron (ETL) and hole (HTL) transport layers, respectively. An organic–inorganic hybrid perovskite (OIHP) crystal has the structure ABX_3 ($A = CH_3$-NH_3^+, $B = Pb^{2+}$, and $X = I^-$, Br^- or Cl^-) [96,172]. In the most commonly used analog of the perovskite, the methylammonium cation sits inside a tetrahedral PbI_2 lattice.

3D OIHPs are well suited to be solar cell absorbers due to their broad absorption band that spans most of the visible region (~350–800 nm), high absorption coefficient ($10^4\ cm^{-1}$ at 550 nm), and low exciton binding energies (10–45 meV) [173]. This means that under illumination at room temperature, OIHPs are likely to generate free charge carriers with no additional energy input [174]. Once the carriers have been produced, the long exciton diffusion length in OIHPs enables effective charge transport [175–179]. On the other hand, careful consideration must be taken to optimize morphology, prevent defects and charge recombination, and promote charge transfer in OIHP solar cells due to the various interfaces present in the device comprising dissimilar materials (i.e., metal oxide/perovskite and perovskite/organic interfaces). Fig. 18 displays representations of the typical device architectures used in conventional n-i-p OIHP solar cells. The ‘i’ is the absorber material sandwiched between an n- and p-type material. In a conventional n-i-p OIHP device structure the typical electrode used is a conductive metal oxide –either ITO or FTO. Atop the electrode is an ETL. This ETL is typically an n-type metal oxide such as TiO_2 or ZnO. As depicted in Fig. 18A, the ETL can be incorporated as a mesoporous scaffold. This porous scaffold is used as structural support as well as a means to increase the surface area interaction with the OIHP. The scaffold also decreases the distance for charges to travel before being transferred, and therefore, reduces chances for bimolecular recombination [180]. There are a few drawbacks encountered when including a porous layer in OIHP solar cells. First, its addition adds another processing step, which increases time and expense and requires high temperatures for particle sintering. Second, the incorporation of metal oxide nanoparticles can lead to changes in the morphology of the OIHP layer, which can produce pinholes and lead to reduced device efficiency. Last, an

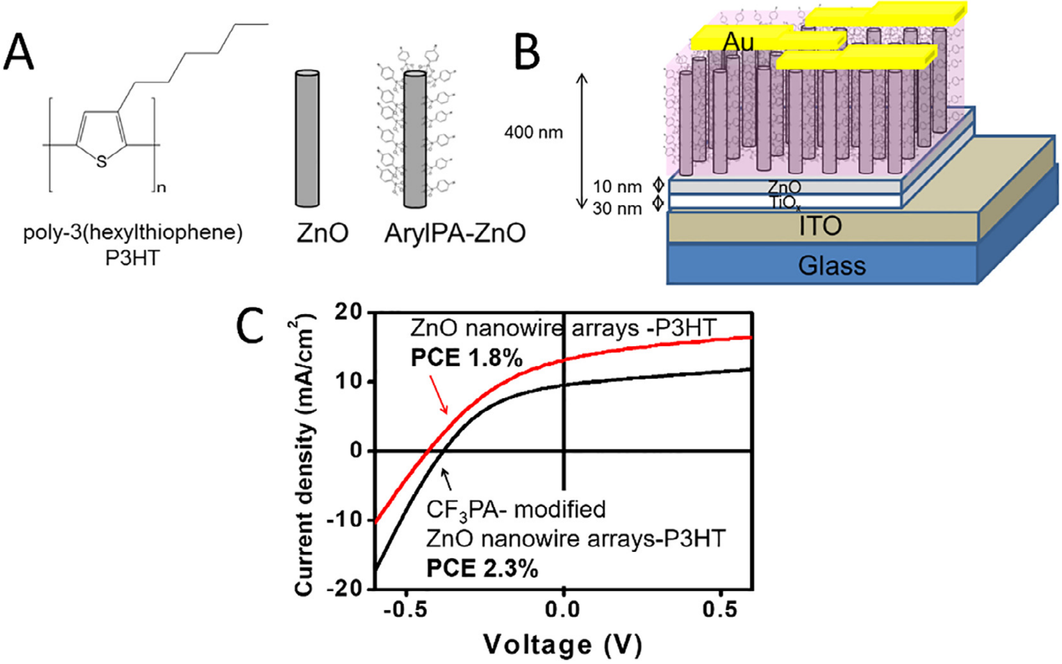

Fig. 17. (A) Chemical structure for the organic donor and schematic depiction of the phosphonate functionalization of a ZnO nanowire. (B) Device architecture used for the assembly of P3HT-SAM functionalized ZnO nanowire arrays inverted solar cells. (C) J–V characteristics for both P3HT:ZnO and P3HT:SAM-functionalized ZnO inverted solar cells.

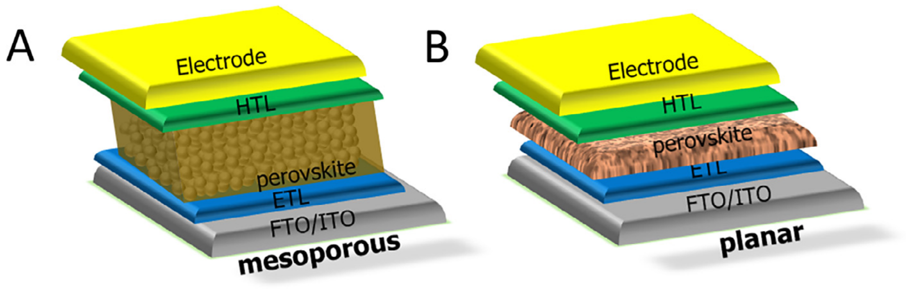

Fig. 18. Schematic representations of the device architecture used in the assembly of conventional perovskite photovoltaics. (A) Mesoporous and (B) planar conventional (n-i-p) perovskite photovoltaics.

increased surface area of the metal oxide comes at the expense of an increased opportunity for surface defects. As discussed earlier, defects in the metal oxide specifically O vacancies produce reduced metal centers that attract and localize holes, leading to assisted electron-hole recombination [61]. Metal oxide ETLs have also been integrated into OIHP photovoltaics as thin films to circumvent issues with fabrication protocols and for reducing pinholes (Fig. 18B) [96]. Above the perovskite, a hole transporting layer (HTL) is deposited (Fig. 18A-B). Typically, this layer is either made of spiro-OMeTAD (2,2′,7,7′-tetrakis(N,N-di-p-methoxyphenylamine)-9,9′-spirobifluorene) or PTAA (poly-triarylamine) films. Metal oxides such as MoO_3 and NiO are the inorganic counterparts of these organic molecules and have, unfortunately, yielded mixed results as they are prone to defects and most solution-processed fabrication methods yield non-uniform films [124,181–184].

Trap-assisted recombination at the metal oxide/OIHP interfaces (both ETL/OIHP and OIHP/HTL interfaces) could detrimentally affect device efficiencies. Chemical modifications via blocking layers or the addition of small molecules and self-assembled monolayers (SAMs) as previously discussed in organic solar cells could aid in defect passivation at these interfaces [78,80,81,185]. For example, a 3-aminopropanoic acid SAM (C_3-SAM) added to a ZnO/$CH_3NH_3PbI_3$ interface not only passivates surface defects but allows for improved OIHP morphology upon solution deposition. In addition, an induced dipole at the interface improves energy level alignment between the ETL and the OIHP. All of these factors lead to an increase in efficiency when compared to a device with no interfacial SAM [81]. Fig. 19A displays a device architecture where SAM modified-ZnO is used as the ETL. Here, the carboxylic group in the C_3-SAM binds to the surface Zn^{2+} ions present in ZnO, creating a monolayer and passivating any defects at the surface. The amino end of the C_3-SAM fits into the OIHP lattice and controls the crystal growth, producing a smoother film. The induced dipole plays a key role in optimizing this device. By lowering the WF of ZnO, it provides better energy level alignment between the ETL and the OIHP, which increases charge transport. Fig. 19B displays the device statistics, where the C_3-SAM functionalized devices (red) have consistently higher power conversion efficiencies than those obtained with devices having unmodified ZnO layers (green) [81]. To this end, the judicious selection of SAM chemistry could enhance surface wettability and control interfacial electronic properties in OIHP photovoltaics.

6.4. Plasmonics

Historically, the study of plasmonic materials has mainly been confined to noble metals such as gold and silver [186]. Plasmonic materials research has also been done with metals like aluminum and copper [187,188]. Due to plasmons dependence on the concentration of free electrons in the material, the field of plasmonics can benefit greatly from the development of novel materials exhibiting tunable carrier concentration and carrier dynamics, as the noble metal plasmonic materials have fixed electron density that cannot be varied post-synthetically [141]. While gold and silver have localized surface plasmon resonances (SPRs) in the visible range; many other metals fall in the UV. Some conducting metal oxides, on the other hand, when post-processed are capable of supporting surface plasmons in the near-IR and mid-IR regions, expanding the range of applications for using plasmonics for sensing, bioimaging, electronics, and solar cells [189,190].

The new applications and technologies available are due to the unique plasmonic properties of metal oxides, primarily created by the ability to control the degree of doping. Controlled doping has long been utilized for metal oxides and other semiconducting materials in order to tailor the materials optical and electronic properties [141]. Dopants result in excess electrons that are avail-

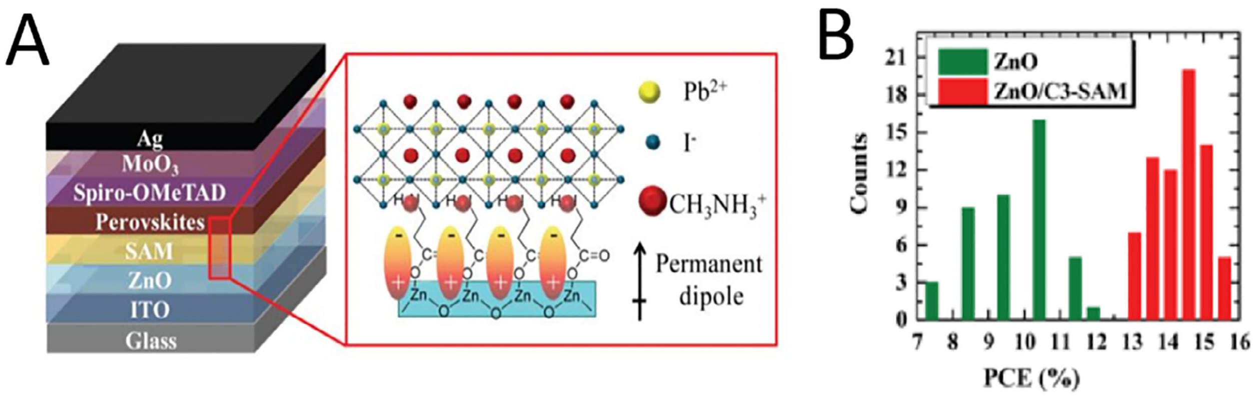

Fig. 19. C_3-SAM functionalized perovskite solar cell. (A) Schematic of a conventional perovskite solar cell and enlarged representation of the C_3-SAM as it passivates defects on the surface of the ZnO ETL and stabilizes the crystallization of the perovskite layer. (B) Device statistics for solar cells fabricated with and without the C_3-SAM. Reprinted with permission from *J. Am. Chem. Soc.*, **2015**, 137, 2674. Copyright (2015) American Chemical Society [81].

able as mobile charge carriers. In the field of plasmonics the collective oscillations of these confined charge carriers resulting from doping in response to incident radiation is what can lead to the SPR.

Plasmonic metal oxides have been successfully utilized in surface-enhanced Raman spectroscopy (SERS). Despite the unique properties of metal oxides, such as their structural versatility and stable exciton formation, their application in SERS has lagged behind Au, Ag, and Cu metal nanostructures due to their weak electromagnetic enhancement and the poor control over nanoparticle polydispersity, size, and shape. Thus, high control over such properties in metal oxides will help control the oscillation frequency to enhance SPRs for the development of nanoantennas or other devices such as plasmonic solar cells. The oscillation frequency and SPRs observed in plasmonic metal or metal oxide nanoparticles suffer from coagulation, high cost, optical loss, limited wavelength, adverse biocompatibility, and selectivity [191]. SERS applications, however, have now evolved into using plasmonic antennas (i.e., plasmonic nanorods) to increase the Raman scattering of molecules coupled to plasmonic surfaces. The increased scattering leads to signal enhancement, which can significantly lower the detection limits for sensing molecules [186]. This technique has opened doors to ZnO-based SERS platforms with the development of various nanostructures. The nanostructures include nanorods, nanowires, nanocones, and nanocages all of which successfully improved the signal with increased scattering [192]. The SERS signal enhancement is shape and size dependent due to the different number of absorption sites for probing molecules, quantum confinement effects, and optical cavity resonance engineering. The ZnO nanostructures are commonly either doped with elements such as cobalt or magnesium or combined with noble metals. The doping of nanostructures can allow for tuning of the localized SPR peak location to the visible region while combining the ZnO nanostructures with noble metals can introduce the opportunity for "hot spot" effects. "Hot spots" enhance sensitivity enabling analysis at the single-molecule level.

With the continued growth of plasmonic metal oxide alternatives, research studies have also found these to be highly suitable for surface-enhanced infrared spectroscopy (SEIRS) [192]. SEIRS is a widely used technique in research and industry as it provides label-free and unambiguous identification of molecular fingerprints. To collect this information, SEIRS relies on the resonant detection of infrared vibrational modes through coupling with the plasmonic modes of an antenna. Wang et al. investigated the strong plasmon confinement of ITO antennas for sub-wavelength SEIRS (Fig. 20) [186]. The long-range transverse interactions observed in ITO antennas were compared to those observed for Au antennas. Fig. 20A depicts three scanning electron micrographs of ITO antenna arrays having different spacings between each antenna. Fig. 20B and C show the infrared transmission spectra for Au and ITO, respectively. The broad concavities observed in the infrared transmission spectra for Au and ITO are due to longitudinal surface plasmon resonances. These resonances (for both Au and ITO) shift to lower energy upon increasing the length of the antennae. Also, ITO antennas show infrared resonances for much shorter antenna lengths when compared to Au antennas. Additionally, regardless of the array spacing, the transmission concavities observed in the IR spectra are less pronounced in ITO than in Au antenna arrays. This suggests that there is a reduced extinction per antenna in ITO when compared to Au antenna arrays. As such,

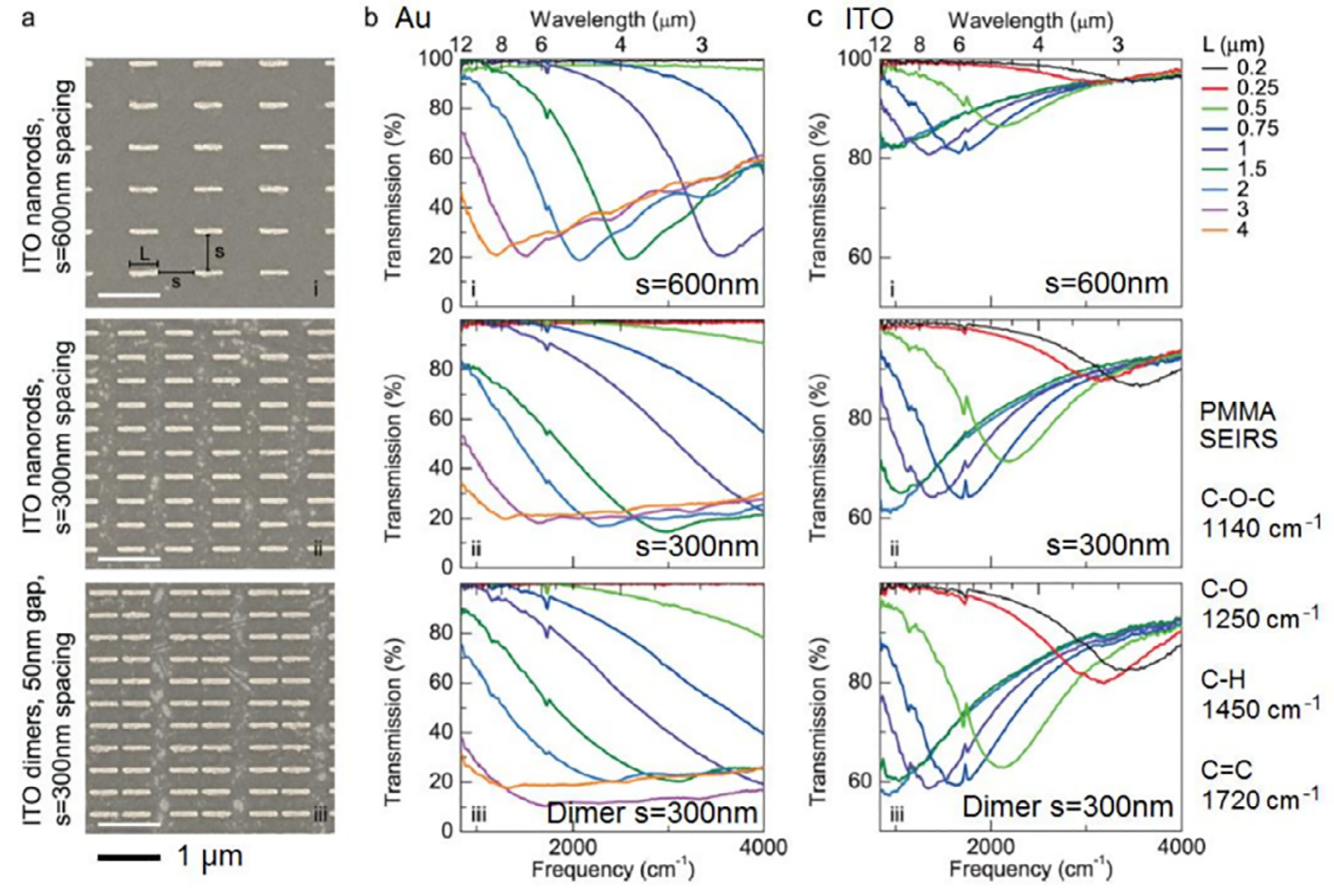

Fig. 20. (A) SEM images of ITO antenna arrays with different antennae spacings. Infrared transmission spectra of Au (B) and ITO (C) antennae arrays as a function of the geometries presented in A. Adapted with permission from *Nano Lett.* **2014**, *14* (1), 346. Copyright 2014 American Chemical Society [186].

there is the promise for using highly-dense ITO antennae arrays for SEIRS with minimal loss in performance, particularly in the mid-infrared.

Biosensing is another application plasmonic metal oxides have been observed to successfully improve performances in by providing very low detection limits. For example, Zhang et al. used 2D hydrogen doped molybdenum oxide (H_xMbO_3) nanodisks to sense glucose at very low concentrations. This was accomplished by varying the amount of hydrogen dopant in the disks; they found that $H_{1.55}MbO_3$ allowed for the most sensitive measurements. Using these disks, they claim to have reached a detection limit lower than any previous plasmonic enzymatic glucose sensor [193]. For $H_{1.55}MbO_3$, they found the detection limit to be 2×10^{-9} M. Additionally, the sensing was done very quickly, within 10 seconds. Perhaps more exciting than the sensing itself, however, is the fact that they were able to easily tune the surface plasmon resonance on the disks across a wide wavelength range. By simply changing the amount of dopant in the metal oxide, they could move the plasmon resonance wavelength between ~400 nm and the near IR. This tunability in doped metal oxides can significantly broaden the range of applications for plasmonic sensing by allowing sensors to be tailored to a specific molecule or event that is being studied.

As indicated in the above applications the plasmon resonances depend strongly on the nanostructure geometry and material. With the growing relevance of plasmonics research for technology, new combinations of plasmonic materials with complementary functionalities are being sought, resulting in improved performances and entirely new application areas.

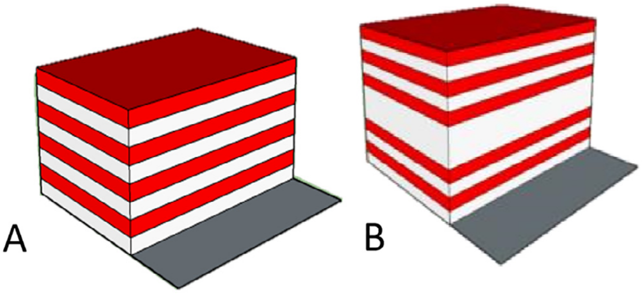

Fig. 21. DBR models. (A) Symmetric structure, alternating high (red) and low (white) refractive index materials. (B) Symmetry-broken DBR structure. A thick, center layer breaks the symmetry of the stack presented in A.

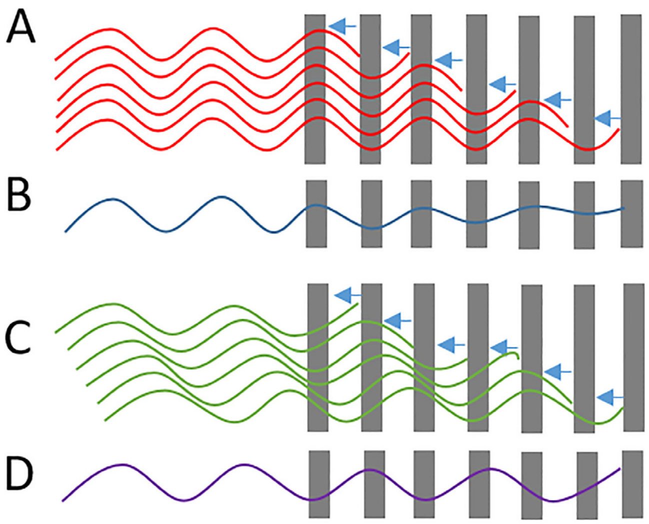

Fig. 22. Optical reflectance and transmittance in a DBR mirror. (A) Wavelengths that are twice the thickness of an optical bilayer enter the DBR and are reflected in-phase. (B) The resulting reflection of a wavelength within the bandgap due to constructive reflection interference. (C) Wavelengths that are longer or shorter than twice the thickness of an optical bilayer enters the DBR and are reflected out-of-phase. (D) The resulting reflection of a wavelength outside the bandgap due to destructive reflection interference.

6.5. Braggs reflectors

Metal oxide semiconductors can also be strategically used in optical devices to create waveguides, mirrors, and sensors. Alternatively, metal oxide optical stacks could also be integrated with optoelectronic devices such as photovoltaics, light emitting diodes, and lasers to improve their performance. For example, it has been demonstrated that the use of one-dimensional photonic bandgap (1D-PGB) structures as distributed Bragg reflectors (DBRs) on the rear end of a solar cell (InGaN/GaN or Si solar cells) increases the external quantum efficiency (total internal reflection of light) in the UV range by reflecting those high energy photons back into the absorber layer. This process dubbed light trapping aid in the enhancement of incident light absorption by the absorber layer thus increasing the generation of the short-circuit current in photovoltaic devices [194–198]. 1D-PGB structures are commonly comprised of alternating multilayer dielectric materials [199]. Commonly, titania (TiO_2) and silica (SiO_2) are alternated in 1D-PGB structures as high and low refractive index materials, respectively. These periodic stacks form DBRs, with characteristic reflection and transmission features. The two major types of DBR designs include symmetric and symmetry broken structures. Fig. 21A displays a model of a symmetric DBR where alternating layers of low and high refractive index material forms a periodic stack. In Fig. 21B, the symmetry of the periodic stack is broken by the addition of a thick layer at the center of the structure. Due to the periodic nature of these materials, DBRs can selectively reflect or transmit certain wavelengths of light. As classically displayed in Fig. 22A, light enters the DBR and a portion of the light is reflected at each interface [200]. As such, reflections from a wavelength that are twice the optical thickness of a bilayer will constructively interfere and be fully reflected (Fig. 22B). A range of wavelengths near this maximum reflectance length will also be reflected, creating a bandgap, typically about 200 nm wide. Alternatively, reflections from wavelengths that are either much shorter or longer than twice the thickness of a bilayer will be reflected out-of-phase, destructively interfering (Fig. 22C), resulting in the transmission of that wavelength (Fig. 22D) [200]. Furthermore, the position of the bandgap can also be estimated using the Bragg-Snell law (Eq. (1)):

$$m\lambda = 2(n_L h_L + n_H h_H) \tag{1}$$

where m = diffraction order, λ = vacuum wavelength of light reflected, n = refractive index, h = physical thickness of layer, L = low n material, H = high n material. The optical thickness of a layer is calculated by multiplying the refractive index of the material by its physical thickness. In this way, the optical thickness of a bilayer can be calculated by simply adding the optical thicknesses of each component. As per Eq. (1), the wavelength reflected by a DBR is twice that of the optical thickness of a bilayer. Therefore, the position of an optical bandgap can be finely controlled by changing the thickness of the alternating layers [201–204].

Similarly, the reflectivity of a DBR within its bandgap is highly dependent on the refractive indices of the low and high n materials as well as the number of bilayers. Eq. (2) enables the calculation of the reflectivity of a DBR:

$$R = \left[\frac{n_o - n_s(n_L/n_H)^{2N}}{n_o + n_s(n_L/n_H)^{2N}}\right]^2 \tag{2}$$

where R = reflectivity, $n_0 = n$ of the environment (air), $n_s = n$ of the substrate, and N = number of bilayers. By analyzing Eq. (2), it can be inferred that there are two ways to increase the reflectivity of a DBR. The first approach involves increasing the number of bilayers (N) [201,204–206]. This will exponentially decrease the second term in Eq. (2) $[n_s(n_L/n_H)]$ and increase reflectivity (R). Fig. 23A displays the evolution of a bandgap structure, by determining the reflectance from 475 to 700 nm, as the number of bilayers in the DBR is increased. With more layers, a sharper, more defined bandgap with high reflectivity is generated. Although this increases reflectivity, interfacial tension and structural cracking have limited the fabrication of DBR structures comprising more than six bilayers. The second method for increasing reflectivity involves increasing the contrast between the high and low n materials, the ratio of (n_L/n_H) (Eq. (2)) or Δn. Since n is a property of a material, an increase in Δn can only be achieved by changing the materials of interest. Fig. 23B shows how changes in Δn affect the reflectivity of the bandgap compared to an archetypical SiO_2/TiO_2 DBR material. As Δn is decreased, the reflectivity decreases and the bandgap structure deteriorates. As Δn is increased, full reflectivity is observed and a sharper bandgap is created. Breaking the DBR symmetry can also affect the bandgap structure. As displayed in Fig. 23C, in a symmetry broken DBR, the insertion of a thicker “defect layer” at the center of the stack allows the transmission of a narrow range of wavelengths. This is dubbed a Fabry-Perot optical cavity [204,207,208].

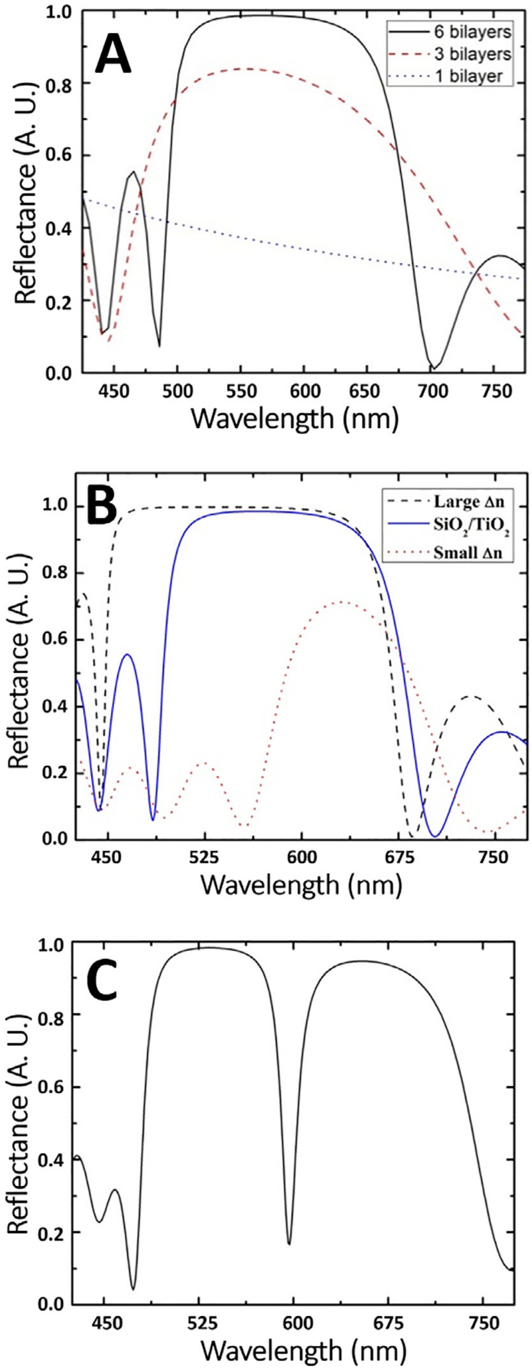

Fig. 23. Simulated reflection spectra of a DBR. (A) Evolution of the bandgap as the number of layers (N) is increased from 1 (dotted) to 3 (dashed) to 6 (solid) bilayers. (B) Change in bandgap as Δn is increased (dashed), where $n_H = 2.08$ and $n_L = 1.21$, or decreased (dotted), where $n_H = 2.08$ and $n_L = 1.8$, from the conventional SiO_2/TiO_2 DBR (solid), where $n_H = 2.08$ and $n_L = 1.47$. (C) A Fabry-Perot optical microcavity around 600 nm, produced by a symmetry broken DBR.

DBRs often have very sharp characteristic bandgaps that enable various applications such as selective coatings, filters [209,210] and waveguides [211]. DBR structures have also been crucial components in many micro-laser designs [212–214]. Recently, DBR structures have attracted much attention since it has been demonstrated that they can be incorporated into liquid and vapor-sensitive sensors and switches [199,215–217]. Liquid and vapor sensitivity can be achieved by the incorporation of mesopores (MPs), pores that are 2–15 nm in diameter and can be infiltrated by fluids, into the structure [199,218]. MP DBR structures have been successfully fabricated via common deposition methods such as atomic layer deposition [219], chemical [220] and physical vapor deposition [221], molecular beam epitaxy [222], and sputtering [223]. Recently, solution-processed deposition of MP DBR materials, such as spin- [224] and dip-coating [199,204,225], have emerged as cheaper and faster alternatives to conventional deposition methods.

Solid DBR structures pose as effective filters and selective coatings due to their bandgap structure having a high, nearly 100% reflectance of specific wavelengths of light [204,209,210]. Another characteristic of an effective filter is steep band-edges on both sides of the bandgap. Shallow band-edges lead to reflection of wavelengths outside of the bandgap and transmission of wavelengths that are intended to be reflected. Filters utilizing a symmetry broken DBR structure require a narrow optical cavity, with a small full width at half maximum (FWHM), to achieve high sensitivity. Broad optical cavities will result in the transmission of a wider range of wavelengths and a reduction in sensitivity. With the high Δn of conventional solid SiO_2/TiO_2 DBR structure, highly reflective, well-defined bandgaps and optical cavities can be achieved [204]. By adding MPs into DBR structures, an active tunability in the bandgap and optical cavity is introduced, allowing MP DBRs to be used as not only filters but also as sensors.

Recently, liquid and vapor sensitive MP DBRs have been developed [199,215–217,221,226–228]. Commonly, MPs are incorporated into a structure by techniques such as anodic etching, molecular beam epitaxy and the layering of nanoparticles. An alternative and less time-consuming method of introducing MPs into DBR material is by the addition of surfactants into a sol–gel precursor solution [150,199,212,229]. With the ability to be infiltrated by liquids and vapors, MPs allow the n of the porous layer to be reversibly tuned after deposition. This change in n upon infiltration of fluids produces detectible and predictable changes in the reflectance bandgap properties allowing these MP DBR materials to act as liquid and vapor sensors [215–217,221,226–228]. In a symmetry-broken DBR sensor, the wavelength of the reflectance minimum is monitored as the fraction of fluid in the MPs changes [230–234]. Similar to all-solid DBRs, the sensitivity of the sensor can be increased by decreasing the FWHM of the reflectance minimum or increasing the reflectivity of the entire film. Both can be accomplished by increasing the number of bilayers and/or Δn. Although effective, current solution-processed MP DBR sensors lack in sensitivity due to a low Δn and the structural instability that results from depositing more than six bilayers. Many of these sensors have narrow or poorly defined bandgaps with broad, large FWHM modes [230–234]. Low Δn results from both materials in the DBR being porous, as portions of both metal oxides are replaced with the same medium; air. This reduces the reflection of the DBR, the steepness of the band-edge and the sensitivity of the sensor. To obtain a larger Δn between the two alternating MP layers, various approaches have been developed, such as alternating pore sizes in each layer [235,236], doping of each layer to change the dielectric properties [236], and alternating MP SiO_2 and MP TiO_2 [224,231]. All of these methods have been successful in increasing the Δn of the DBR. However, the increase is not sufficient to produce a complete bandgap structure in the transmission or reflection spectra. Further, structural stability issues have prevented deposition of more than six bilayers, requiring an increase in Δn to achieve any further increase in reflectivity or bandgap definition.

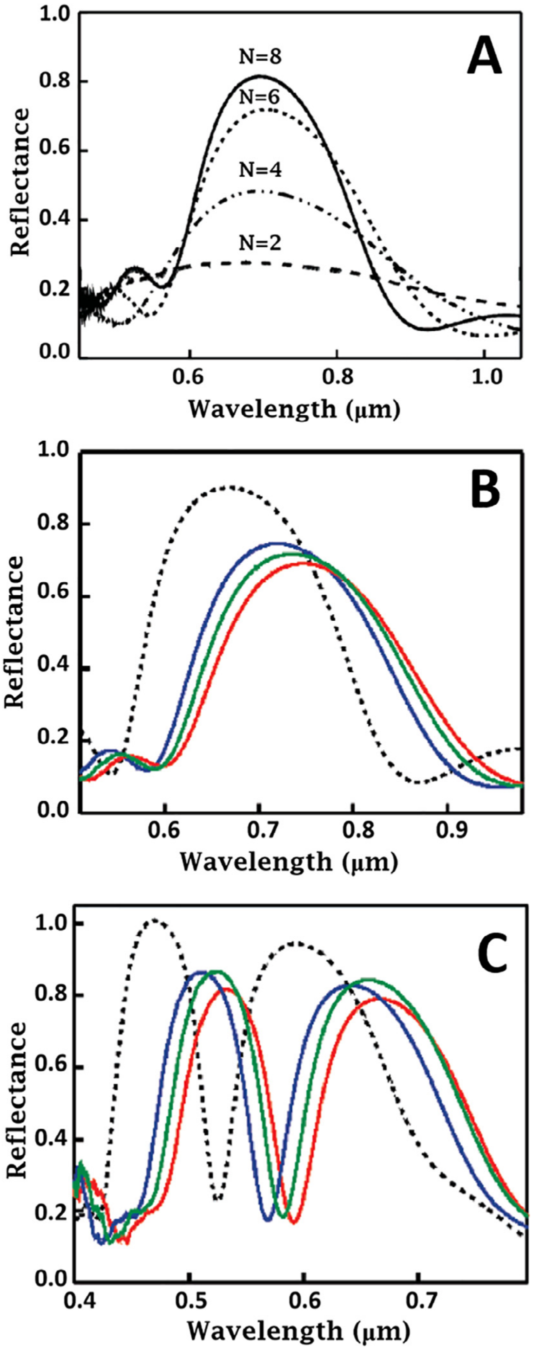

Fig. 24. Reflectance spectra of all-MP DBRs. (A) Evolution of reflectance bandgap in an all-MP SiO_2/TiO_2 DBR as the number of layers is increased. (B) Response of the same MP DBR as it is infiltrated with different refractive index liquids (black dot = pristine, blue = water, green = ethylene glycol, red = Chlorobenzene). (C) Response of a symmetry broken all-MP DBR as it is infiltrated with the same solvents as in B. Reprinted with permission from *Langmuir* **2008**, *24* (9), 4430. Copyright (2008) American Chemical Society [234]. (Colour online.)

Attempts to improve the reflectivity of MP DBR sensors have focused on the fabrication of all-MP DBR structures. Using conventional materials to create a DBR structure, attempts have been made to create DBRs alternating MP TiO_2 as the high n material and MP SiO_2 as the low n material [224,233,234]. The highest reflectivity reached with these materials is approximately 60–80%, with a poorly defined bandgap. Fig. 24A displays the reflectance bandgap characteristics as layers are added to an all-MP SiO_2/TiO_2 DBR [233]. Similar results were obtained by Guldin et al. by alternating the porosity in each layer of an all-MP TiO_2 DBR [235]. These bandgap structures are narrow with shallow band-edges, and although they show a response to infiltration (Fig. 24B), they lack sensitivity.

The most highly sensitive optical cavity-based sensors, displaying sensitivity to liquids [233] and vapors [233] were reported by Colodrero et al. and displays a FWHM of about 40 nm (Fig. 24C) [233,234]. Optical cavities with FWHM values of about 45 nm have been achieved by changing the porosity and selectively functionalizing one of the alternating layers [231]. All SiO_2 and all-TiO_2 DBRs have been made using a similar procedure of changing the porosity of each alternating layer [235]. This method successfully increases the reflectivity of these systems. However, the production of a fully defined bandgap using this method has not been reported [231,235]. Another approach to manipulate the refractive index involves making solid solutions of TiO_2 layers with various ratios of Al_2O_3 and SiO_2 [236]. This method has effectively produced the highest reported Δn value of about 0.25 in an all-MP doped-TiO_2 DBR sensor, but a full bandgap structure has not yet been reported [236]. By manipulating the fraction of Al_2O_3 and SiO_2 within the alternating layers of an all-MP DBR, Ghazzal et al. were able to create a switching device that decreases in transmission upon infiltration [236]. Fig. 25 displays the transmission spectra of the switch fabricated by Ghazzal et al. Upon infiltration of this

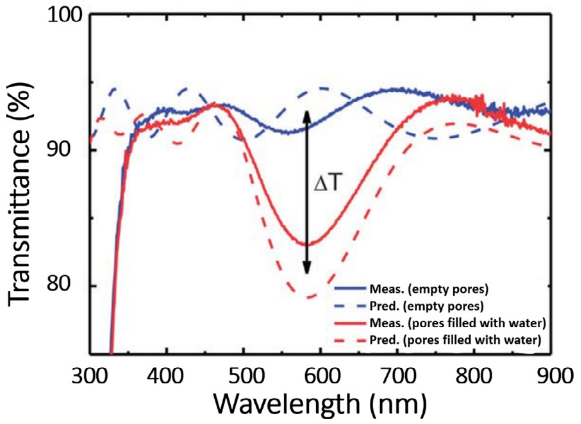

Fig. 25. Simulated and experimental transmission spectra of an MP DBR before (red) and after (blue) infiltration of pores with water. Upon infiltration, an approximately 9% change in the transmission is observed. Reproduced from *J. Mater. Chem. C* **2013**, *1* (39), 6202–6209 with permission of The Royal Society of Chemistry [236]. (Colour online.)

MP DBR, a reduction in transmission of approximately 9% is observed at 600 nm, creating an optical "switch" [236]. Although previous work displays response of MP DBRs to liquids and vapors, significant progress needs to be made in this area to increase the reflectivity and sensitivity of DBRs containing metal oxides to a point where they could be effective sensors.

7. Summary, opportunities, and challenges

This review provides a comprehensive study on recent advances in the fabrication, characterization, and device application of metal oxide nanostructures and thin films. As we cannot conceivably cover a century worth of research on metal oxides without breaking editorial rules and being mentally (and perhaps physically) exhausted, we decided to mainly focus this review on their applicability towards energy conversion technologies. Besides applications, we also present a very detailed discussion on how fabrication procedures can affect the morphology, stoichiometry, defects, and electronic structures of metal oxides. Current research efforts have mostly focused on fabricating metal oxide p-n heterojunctions containing either inorganic or semiconducting components. With the design of such hybrid structures and interfaces, it is possible to enable unique physical and chemical properties not found in either of the pure constituents. This often results in enhanced performance when incorporated into functional devices.

Although great attention has been centered on the development of novel metal oxide structures as well as understanding the interaction between metal oxide-metal oxide and metal oxide-organic interfaces, many challenges remain. First, the lack of atomic precision during the synthesis of metal oxide nanostructures results in increased size distribution, polydispersity, and poor morphology control. As such, eliminating broad size distributions and polydispersity will reduce variations in the observed physical and chemical properties of metal oxide nanostructures. This will allow for more controlled and reproducible device characteristics. We believe a paradigm-shifting approach involving a well-developed mechanistic understanding of how the interplay between kinetics and thermodynamics affect the synthesis of metal oxide nanostructures is urgently needed. Second, the quality of the metal oxide-metal oxide and metal oxide-organic interfaces in p-n heterojunctions needs to be improved as well as understood (i.e., control over crystallinity, morphology, dangling bonds, surface energetics). Beyond the physical characteristics of the interface, the electronic properties also need to be investigated more in-depth. Utilizing some of the in situ characterization tools (i.e., in situ X-ray photoelectron spectroscopy, in situ transmission electron microscopy, and in situ X-ray absorption fine structure spectroscopy) developed for understanding electrochemical reactions in energy conversion processes could help in the elucidation of how interfaces involving metal oxides are formed both kinetically and thermodynamically.

Acknowledgments

The authors would like to acknowledge support from the National Science Foundation (USA) under Award# DMR 1824263. L.W.B. would also like to acknowledge financial support from the Research Corporation for Science Advancement (USA) through a Cottrell Scholar Award and a Scialog Collaborative Innovation Award.

References

[1] M.-G. Kim, M.G. Kanatzidis, A. Facchetti, T.J. Marks, Low-temperature fabrication of high-performance metal oxide thin-film electronics via combustion processing, Nat. Mater. 10 (2011) 382.
[2] X. Yu, T.J. Marks, A. Facchetti, Metal oxides for optoelectronic applications, Nat. Mater. 15 (2016) 383.
[3] L.L. Hench, J.K. West, The sol–gel process, Chem. Rev. 90 (1990) 33.
[4] A.P.A. Oliveira, J.-F. Hochepied, F. Grillon, M.-H. Berger, Controlled precipitation of zinc oxide particles at room temperature, Chem. Mater. 15 (2003) 3202.
[5] K. Okuyama, Y. Kousaka, N. Tohge, S. Yamamoto, J.J. Wu, R.C. Flagan, J.H. Seinfeld, Production of ultrafine metal oxide aerosol particles by thermal decomposition of metal alkoxide vapors, AIChE J. 32 (1986) 2010.
[6] T. Adschiri, Y. Hakuta, K. Arai, Hydrothermal synthesis of metal oxide fine particles at supercritical conditions, Ind. Eng. Chem. Res. 39 (2000) 4901.
[7] S.M. Liu, L.M. Gan, L.H. Liu, W.D. Zhang, H.C. Zeng, Synthesis of single-crystalline TiO_2 nanotubes, Chem. Mater. 14 (2002) 1391.
[8] P.-C. Chang, Z. Fan, D. Wang, W.-Y. Tseng, W.-A. Chiou, J. Hong, J.G. Lu, ZnO nanowires synthesized by vapor trapping CVD method, Chem. Mater. 16 (2004) 5133.
[9] A.J. Ben-Sasson, G. Ankonina, M. Greenman, M.T. Grimes, N. Tessler, Low-temperature molecular vapor deposition of ultrathin metal oxide dielectric for low-voltage vertical organic field effect transistors, ACS Appl. Mater. Interfaces 5 (2013) 2462.
[10] D.G. Schlom, Perspective: Oxide molecular-beam epitaxy rocks!, APL Mater 3 (2015) 062403.
[11] W.A. Doolittle, A.G. Carver, W. Henderson, Molecular beam epitaxy of complex metal-oxides: Where have we come, where are we going, and how are we going to get there?, J Vac. Sci. Technol. B 23 (2005) 1272.
[12] F. Baiutti, G. Christiani, G. Logvenov, Towards precise defect control in layered oxide structures by using oxide molecular beam epitaxy, Beilstein J. Nanotechnol. 5 (2014) 596.
[13] R.B. Comes, P.V. Sushko, S.M. Heald, R.J. Colby, M.E. Bowden, S.A. Chambers, Band-gap reduction and dopant interaction in epitaxial La, Cr Co-doped $SrTiO_3$ thin films, Chem. Mater. 26 (2014) 7073.
[14] J. Puetz, M.A. Aergerter, Dip coating technique, in: M.A. Aegerter, M. Mennig (Eds.), Sol–gel technologies for glass producers and users, Springer, Boston, MA, 2004.
[15] V.K. Champagne, The Cold Spray Materials Deposition Process: Fundamentals and Applications, CRC Press, Cambridge: Woodhead; Boca Raton, 2007.
[16] T. Kaneda, D. Hirose, T. Miyasako, P.T. Tue, Y. Murakami, S. Kohara, J. Li, T. Mitani, E. Tokumitsu, T. Shimoda, Rheology printing for metal-oxide patterns and devices, J. Mater. Chem. C 2 (2013) 40.
[17] J. Perelaer, P.J. Smith, D. Mager, D. Soltman, S.K. Volkman, V. Subramanian, J.G. Korvink, U.S. Schubert, Printed electronics: The challenges involved in printing devices, interconnects, and contacts based on inorganic materials, J. Mater. Chem. 20 (2010) 8446.
[18] C. Drosos, D. Vernardou, Advancements, challenges and prospects of chemical vapour pressure at atmospheric pressure on vanadium dioxide structures, Materials 11 (2018) 1.
[19] C.E. Knapp, C.J. Carmalt, Solution based CVD of main group materials, Chem. Soc. Rev. 45 (2016) 1036.
[20] A.M.B. van Mol, Y. Chae, A.H. McDaniel, M.D. Allendorf, Chemical vapor deposition of tin oxide: fundamentals and applications, Thin Solid Films 502 (2006) 72.
[21] T. Kodas, M.J. Hampden-Smith, The Chemistry of Metal CVD, VCH, Weinheim; New York, 1994.
[22] A.C. Dunbar, G.S. Girolami, Synthesis and characterization of calcium N, N-dimethylaminodiboranates as possible chemical vapor deposition precursors, Inorg. Chem. 53 (2014) 888.
[23] W.B. Wang, N.N. Chang, T.A. Codding, G.S. Girolami, J.R. Abelson, Superconformal chemical vapor deposition of thin films in deep features, J. Vac. Sci. Technol. A 32 (2014) 051512.
[24] R.W. Johnson, A. Hultqvist, S.F. Bent, A brief review of atomic layer deposition: from fundamentals to applications, Mater. Today 17 (2014) 236.
[25] M.A. Herman, Molecular Beam Epitaxy: Fundamentals and Current Status, second rev. and updated ed., Springer, Berlin, New York, 1996.
[26] R. Viter, I. Baleviciute, A. Abou Chaaya, L. Mikoliunaite, Z. Balevicius, A. Ramanavicius, A. Zalesska, V. Vataman, V. Smyntyna, Z. Gertnere, D. Erts, P. Miele, M. Bechelany, Optical properties of ultrathin Al_2O_3/ZnO nanolaminates, Thin Solid Films 594 (2015) 96.
[27] Y. Wang, P. Miska, D. Pilloud, D. Horwat, F. Mücklich, J.F. Pierson, Transmittance enhancement and optical band gap widening of Cu_2O thin films after air annealing, J. Appl. Phys. 115 (2014) 073505.
[28] J. Cui, Temperature dependent photoluminescence with spontaneous piezoelectric field in $ZnO/Zn_{0.74}Mg_{0.26}O$ single quantum wells, Appl. Phys. Lett. 90 (2007) 031905.
[29] L. Wang, N.C. Giles, Temperature dependence of the free-exciton transition energy in zinc oxide by photoluminescence excitation spectroscopy, J. Appl. Phys. 94 (2003) 973.
[30] D. Rudolph, L. Schweickert, S. Morkötter, L. Hanschke, S. Hertenberger, M. Bichler, G. Koblmüller, G. Abstreiter, J.J. Finley, Probing the trapping and thermal activation dynamics of excitons at single twin defects in GaAs–AlGaAs core–shell nanowires, New J. Phys. 15 (2013) 113032.
[31] T. Lu, Z. Ma, C. Du, Y. Fang, H. Wu, Y. Jiang, L. Wang, L. Dai, H. Jia, W. Liu, H. Chen, Temperature-dependent photoluminescence in light-emitting diodes, Sci. Rep. 4 (2014) 6131.
[32] K. Das, S.N. Sharma, M. Kumar, S.K. De, Morphology dependent luminescence properties of Co doped TiO_2 nanostructures, J. Phys. Chem. C 113 (2009) 14783.

[33] A.R. Gheisi, C. Neygandhi, A.K. Sternig, E. Carrasco, H. Marbach, D. Thomele, O. Diwald, O_2 adsorption dependent photoluminescence emission from metal oxide nanoparticles, Phys. Chem. Chem. Phys. 16 (2014) 23922.

[34] T. Lin, X. Lv, S. Li, Q. Wang, The morphologies of the semiconductor oxides and their gas-sensing properties, Sensors 17 (2017) 1.

[35] A. Hexemer, P. Muller-Buschbaum, Advanced grazing-incidence techniques for modern soft-matter materials analysis (Report), IUCrJ 2 (2015) 106.

[36] D. Altamura, T. Sibillano, D. Siliqi, L. De Caro, C. Giannini, Assembled nanostructured architectures studied by grazing incidence X-ray scattering, Nanomater. Nanotechnol. 2 (2012) 1.

[37] W. Zeng, X. Liu, X. Guo, Q. Niu, J. Yi, R. Xia, Y. Min, Morphology analysis and optimization: crucial factor determining the performance of perovskite solar cells, Molecules 22 (2017) 1.

[38] G. Liu, W. Jaegermann, J. He, V. Sundström, L. Sun, XPS and UPS characterization of the TiO_2/ZnPcGly heterointerface: alignment of energy levels, J. Phys. Chem. B 106 (2002) 5814.

[39] A. Kuzmin, J. Chaboy, EXAFS and XANES analysis of oxides at the nanoscale, IUCrJ 1 (2014) 571.

[40] J. Zhang, M. Zhang, R.-Q. Sun, X. Wang, A facile band alignment of polymeric carbon nitride semiconductors to construct isotype heterojunctions, Angew. Chem., Int. Ed. 51 (2012) 10145.

[41] A. Degrauw, R. Armstrong, A.A. Rahman, J. Ogle, L. Whittaker-Brooks, Catalytic growth of vertically aligned SnS/SnS_2 p-n heterojunctions, Mater. Res. Express 4 (2017) 094002.

[42] M.S. Lundstrom, Boundary conditions for pn heterojunctions, Solid State Electron. 27 (1984) 491.

[43] S.S. Perlman, D.L. Feucht, p-n heterojunctions, Solid State Electron. 7 (1964) 911.

[44] J. Liu, L. Ruan, S.B. Adeloju, Y. Wu, BiOI/TiO_2 nanotube arrays, a unique flake-tube structured p-n junction with remarkable visible-light photoelectrocatalytic performance and stability, Dalton Trans. 43 (2014) 1706.

[45] X. Xue, L. Xing, Y. Chen, S. Shi, Y. Wang, T. Wang, Synthesis and H_2S sensing properties of CuO–SnO_2 core/shell pn-junction nanorods, J. Phys. Chem. C 112 (2008) 12157.

[46] Z. Zhang, C. Shao, X. Li, C. Wang, M. Zhang, Y. Liu, Electrospun nanofibers of p-type NiO/n-type ZnO heterojunctions with enhanced photocatalytic activity, ACS Appl. Mater. Interfaces 2 (2010) 2915.

[47] Q. Li, S. Ding, W. Zhu, L. Feng, H. Dong, W. Hu, Recent advances in one-dimensional organic p-n heterojunctions for optoelectronic device applications, J. Mater. Chem. C 4 (2016) 9388.

[48] Z. Wang, X. Zhan, Y. Wang, M. Safdar, M. Niu, J. Zhang, Y. Huang, J. He, ZnO/ZnS_xSe_{1-x} core/shell nanowire arrays as photoelectrodes with efficient visible light absorption, Appl. Phys. Lett. 101 (2012) 073105.

[49] H. Yu, S. Chen, X. Quan, H. Zhao, Y. Zhang, Silicon nanowire/TiO_2 heterojunction arrays for effective photoelectrocatalysis under simulated solar light irradiation, Appl. Catal. B 90 (2009) 242.

[50] Y. Myung, D.M. Jang, T.K. Sung, Y.J. Sohn, G.B. Jung, Y.J. Cho, H.S. Kim, J. Park, Composition-tuned ZnO-CdSSe core-shell nanowire arrays, ACS Nano 4 (2010) 3789.

[51] D.S. Shin, I. Cho, T.G. Kim, S.H. Jeong, J. Park, Investigation of p-CuO/n-$Cu_{1-x}In_xO$ core/shell nanowire structure performance in UV photodetectors, J. Alloys Compd. 728 (2017) 1180.

[52] Y. Peng, M. Yan, Q.-G. Chen, C.-M. Fan, H.-Y. Zhou, A.-W. Xu, Novel one-dimensional Bi_2O_3–Bi_2WO_6 p-n hierarchical heterojunction with enhanced photocatalytic activity, J. Mater. Chem. A 2 (2014) 8517.

[53] A. Rabenau, The role of hydrothermal synthesis in preparative chemistry, Angew. Chem., Int. Ed. 24 (1985) 1026.

[54] A.L. Briseno, T.W. Holcombe, A.I. Boukai, E.C. Garnett, S.W. Shelton, J.J.M. Fréchet, P. Yang, Oligo- and polythiophene/ZnO hybrid nanowire solar cells, Nano Lett. 10 (2010) 334.

[55] C. Martini, G. Poize, D. Ferry, D. Kanehira, N. Yoshimoto, J. Ackermann, F. Fages, Oligothiophene self-assembly on the surface of ZnO nanorods: toward coaxial p-n hybrid heterojunctions, ChemPhysChem 10 (2009) 2465.

[56] C.N.R. Rao, Transition Metal Oxides, VCH, New York, 1995.

[57] C.W. Kwon, A. Poquet, S. Mornet, G. Campet, M.H. Delville, M. Treguer, J. Portier, Electronegativity and chemical hardness: two helpful concepts for understanding oxide nanochemistry, Mater. Lett. 51 (2001) 402.

[58] R.G. Parr, R.G. Pearson, Absolute hardness: companion parameter to absolute electronegativity, J. Am. Chem. Soc. 105 (1983) 7512.

[59] P. Ayers, R.G. Parr, R.G. Pearson, Elucidating the hard/soft acid/base principle: a perspective based on half-reactions, J. Chem. Phys. 124 (2006).

[60] S.F. Matar, G. Campet, M.A. Subramanian, Electronic properties of oxides: chemical and theoretical approaches, Prog. Solid State Chem. 39 (2011) 70.

[61] M.T. Greiner, Z.-H. Lu, Thin-film metal oxides in organic semiconductor devices: their electronic structures, work functions and interfaces, Npg Asia Mater. 5 (2013) e55.

[62] R.A. John, N.A. Chien, S. Shukla, N. Tiwari, C. Shi, N.G. Ing, N. Mathews, Low-temperature chemical transformations for high-performance solution-processed oxide transistors, Chem. Mater. 28 (2016) 8305.

[63] B. Jiang, J.M. Zuo, N. Jiang, M. O'Keeffe, J.C.H. Spence, Charge density and chemical bonding in rutile, TiO_2, Acta Crystallogr., Sect. A 59 (2003) 341.

[64] K. Nomura, H. Ohta, A. Takagi, T. Kamiya, M. Hirano, H. Hosono, Room-temperature fabrication of transparent flexible thin-film transistors using amorphous oxide semiconductors, Nature 432 (2004) 488.

[65] J.S. Park, W.-J. Maeng, H.-S. Kim, J.-S. Park, Review of recent developments in amorphous oxide semiconductor thin-film transistor devices, Thin Solid Films 520 (2012) 1679.

[66] S.R. Thomas, P. Pattanasattayavong, T.D. Anthopoulos, Solution-processable metal oxide semiconductors for thin-film transistor applications, Chem. Soc. Rev. 42 (2013) 6910.

[67] P.F. Carcia, R.S. McLean, M.H. Reilly, G. Nunes, Transparent ZnO thin-film transistor fabricated by rf magnetron sputtering, Appl. Phys. Lett. 82 (2003) 1117.

[68] Y.-H. Lin, H. Faber, K. Zhao, Q. Wang, A. Amassian, M. McLachlan, T.D. Anthopoulos, High-performance ZnO transistors processed via an aqueous carbon-free metal oxide precursor route at temperatures between 80–180°C, Adv. Mater. 25 (2013) 4340.

[69] B.S. Ong, C. Li, Y. Li, Y. Wu, R. Loutfy, Stable, Solution-processed, high-mobility ZnO thin-film transistors, J. Am. Chem. Soc. 129 (2007) 2750.

[70] K. Hong, S.H. Kim, K.H. Lee, C.D. Frisbie, Printed, sub-2V ZnO electrolyte gated transistors and inverters on plastic, Adv. Mater. 25 (2013) 3413.

[71] A. Bashir, P.H. Wöbkenberg, J. Smith, J.M. Ball, G. Adamopoulos, D.D.C. Bradley, T.D. Anthopoulos, High-performance zinc oxide transistors and circuits fabricated by spray pyrolysis in ambient atmosphere, Adv. Mater. 21 (2009) 2226.

[72] M.T. Greiner, M.G. Helander, W.-M. Tang, Z.-B. Wang, J. Qiu, Z.-H. Lu, Universal energy-level alignment of molecules on metal oxides, Nat. Mater. 11 (2011) 76.

[73] A.H. Nethercot, Prediction of Fermi energies and photoelectric thresholds based on electronegativity concepts, Phys. Rev. Lett. 33 (1974) 1088.

[74] M.T. Greiner, L. Chai, M.G. Helander, W.-M. Tang, Z.-H. Lu, Transition metal oxide work functions: the influence of cation oxidation state and oxygen vacancies, Adv. Funct. Mater. 22 (2012) 4557.

[75] K. Nomura, H. Ohta, K. Ueda, T. Kamiya, M. Hirano, H. Hosono, Thin-film transistor fabricated in single-crystalline transparent oxide semiconductor, Science 300 (2003) 1269.

[76] X. Liang, S. Bai, X. Wang, X. Dai, F. Gao, B. Sun, Z. Ning, Z. Ye, Y. Jin, Colloidal metal oxide nanocrystals as charge transporting layers for solution-processed light-emitting diodes and solar cells, Chem. Soc. Rev. 46 (2017) 1730.

[77] L. Liu, A. Mei, T. Liu, P. Jiang, Y. Sheng, L. Zhang, H. Han, Fully printable mesoscopic perovskite solar cells with organic silane self-assembled monolayer, J. Am. Chem. Soc. 137 (2015) 1790.

[78] H. Zhou, Q. Chen, G. Li, S. Luo, T.-B. Song, H.-S. Duan, Z. Hong, J. You, Y. Liu, Y. Yang, Interface engineering of highly efficient perovskite solar cells, Science 345 (2014) 542.

[79] Y.C. Kim, T.Y. Yang, N.J. Jeon, J. Im, S. Jang, T.J. Shin, H.W. Shin, S. Kim, E. Lee, S. Kim, J.H. Noh, S.I. Seok, J. Seo, Engineering interface structures between lead halide perovskite and copper phthalocyanine for efficient and stable perovskite solar cells, Energy Environ. Sci. 10 (2017) 2109.

[80] L. Whittaker-Brooks, W.E. McClain, J. Schwartz, Y.-L. Loo, Donor-acceptor interfacial interactions dominate device performance in hybrid P3HT-ZnO nanowire-array solar cells, Adv. Energy Mater. 4 (2014) 1400585.

[81] L. Zuo, Z. Gu, T. Ye, W. Fu, G. Wu, H. Li, H. Chen, Enhanced photovoltaic performance of $CH_3NH_3PbI_3$ perovskite solar cells through interfacial engineering using self-assembling monolayer, J. Am. Chem. Soc. 137 (2015) 2674.

[82] Y. Rong, Y. Hu, S. Ravishankar, H. Liu, X. Hou, Y. Sheng, A. Mei, Q. Wang, D. Li, M. Xu, J. Bisquert, H. Han, Tunable hysteresis effect for perovskite solar cells, Energy Environ. Sci. 10 (2017) 2383.

[83] M. Nolan, G.W. Watson, The electronic structure of alkali doped alkaline earth metal oxides: Li doping of MgO studied with DFT-GGA and GGA+U, Surf. Sci. 586 (2005) 25.

[84] H.J. Lee, S.-H. Shin, K.T. Nam, J. Nah, M.H. Lee, Spontaneously polarized lithium-doped zinc oxide nanowires as photoanodes for electrical water splitting, J. Mater. Chem. A 4 (2016) 3223.

[85] M.-H. Park, J.-H. Li, A. Kumar, G. Li, Y. Yang, Doping of the metal oxide nanostructure and its influence in organic electronics, Adv. Funct. Mater. 19 (2009) 1241.

[86] E. Polydorou, A. Zeniou, D. Tsikritzis, A. Soultati, I. Sakellis, S. Gardelis, T.A. Papadopoulos, J. Briscoe, L.C. Palilis, S. Kennou, E. Gogolides, P. Argitis, D. Davazoglou, M. Vasilopoulou, Surface passivation effect by fluorine plasma treatment on ZnO for efficiency and lifetime improvement of inverted polymer solar cells, J. Mater. Chem. A 4 (2016) 11844.

[87] C.J. Flynn, S.M. McCullough, E. Oh, L. Li, C.C. Mercado, B.H. Farnum, W. Li, C.L. Donley, W. You, A.J. Nozik, J.R. McBride, T.J. Meyer, Y. Kanai, J.F. Cahoon, Site-selective passivation of defects in NiO solar photocathodes by targeted atomic deposition, ACS Appl. Mater. Interfaces 8 (2016) 4754.

[88] Y. Huang, Q. Zhang, J. Xi, Z. Ji, Transparent conductive p-type lithium-doped nickel oxide thin films deposited by pulsed plasma deposition, Appl. Surf. Sci. 258 (2012) 7435.

[89] H. Sato, T. Minami, S. Takata, T. Yamada, Transparent conducting p-type NiO thin films prepared by magnetron sputtering, Thin Solid Films 236 (1993) 27.

[90] J.R. Manders, S.-W. Tsang, M.J. Hartel, T.-H. Lai, S. Chen, C.M. Amb, J.R. Reynolds, F. So, Solution-processed nickel oxide hole transport layers in high efficiency polymer photovoltaic cells, Adv. Funct. Mater. 23 (2013) 2993.

[91] S.C. Chen, C.K. Wen, T.Y. Kuo, W.C. Peng, H.C. Lin, Characterization and properties of NiO films produced by rf magnetron sputtering with oxygen ion source assistance, Thin Solid Films 572 (2014) 51.

[92] Z. Wang, P.K. Nayak, J.A. Caraveo-Frescas, H.N. Alshareef, Recent developments in p-type oxide semiconductor materials and devices, Adv. Mater. 28 (2016) 3831.

[93] F.P. Koffyberg, F.A. Benko, A photoelectrochemical determination of the position of the conduction and valence band edges of p-type CuO, J. Appl. Phys. 53 (1982) 1173.

[94] S.V. Ovsyannikov, A.E. Karkin, N.V. Morozova, V.V. Shchennikov, E. Bykova, A. M. Abakumov, A.A. Tsirlin, K.V. Glazyrin, L. Dubrovinsky, A Hard oxide semiconductor with a direct and narrow bandgap and switchable p-n electrical conduction, Adv. Mater. 26 (2014) 8185.

[95] A.V. Emeline, G.V. Kataeva, A.V. Panasuk, V.K. Ryabchuk, N.V. Sheremetyeva, N. Serpone, Effect of surface photoreactions on the photocoloration of a wide band gap metal oxide: probing whether surface reactions are photocatalytic, J. Phys. Chem. B 109 (2005) 5175.

[96] W.J. Nimens, J. Ogle, A. Caruso, M. Jonely, C. Simon, D. Smilgies, R. Noriega, M. Scarpulla, L. Whittaker-Brooks, Morphology and optoelectronic variations underlying the nature of the electron transport layer in perovskite solar cells, ACS Appl. Energy Mater. 1 (2018) 602.

[97] L. Whittaker-Brooks, J.M. Mativetsky, A. Woll, D. Smilgies, Y.-L. Loo, Sputtered ZnO seed layer enhances photovoltaic behavior in hybrid ZnO/P3HT solar cells, Org. Electron. 14 (2013) 3477.

[98] V. Srikant, D.R. Clarke, On the optical band gap of zinc oxide, J. Appl. Phys. 83 (1998) 5447.

[99] T. Onuma, S. Saito, K. Sasaki, T. Masui, T. Yamaguchi, T. Honda, M. Higashiwaki, Valence band ordering in β-Ga_2O_3 studied by polarized transmittance and reflectance spectroscopy, Jpn. J. Appl. Phys. 54 (2015) 112601.

[100] E.O. Filatova, A.S. Konashuk, Interpretation of the changing the band gap of Al_2O_3 depending on its crystalline form: connection with different local symmetries, J. Phys. Chem. C 119 (2015) 20755.

[101] M. Gutowski, J.E. Jaffe, C.-L. Liu, M. Stoker, R.I. Hegde, R.S. Rai, P.J. Tobin, Thermodynamic stability of high-K dielectric metal oxides ZrO_2 and HfO_2 in contact with Si and SiO_2, Appl. Phys. Lett. 80 (2002) 1897.

[102] B.M. Hudak, S.W. Depner, G.R. Waetzig, A. Talapatra, R. Arroyave, S. Banerjee, B.S. Guiton, Real-time atomistic observation of structural phase transformations in individual hafnia nanorods, Nat. Commun. 8 (2017) 15316.

[103] G.R. Waetzig, S.W. Depner, H. Asayesh-Ardakani, N.D. Cultrara, R. Shahbazian-Yassar, S. Banerjee, Stabilizing metastable tetragonal HfO_2 using a non-hydrolytic solution-phase route: ligand exchange as a means of controlling particle size, Chem. Sci. 7 (2016) 4930.

[104] G. Mavrou, S. Galata, P. Tsipas, A. Sotiropoulos, Y. Panayiotatos, A. Dimoulas, E.K. Evangelou, J.W. Seo, C. Dieker, Electrical properties of La_2O_3 and HfO_2/La_2O_3 gate dielectrics for germanium metal-oxide-semiconductor devices, J. Appl. Phys. 103 (2008) 014506.

[105] X. Su, Z. Zhang, M. Zhu, Melting and optical properties of ZnO nanorods, Appl. Phys. Lett. 88 (2006) 061913.

[106] D.R. Rosseinsky, R.J. Mortimer, Electrochromic systems and the prospects for devices, Adv. Mater. 13 (2001) 783.

[107] M. Zheng, H. Tang, L. Li, Q. Hu, L. Zhang, H. Xue, H. Pang, Hierarchically nanostructured transition metal oxides for lithium-ion batteries, Adv. Sci. 5 (2018) 1700592.

[108] H.B. Wu, J.S. Chen, H.H. Hng, X. Wen Lou, Nanostructured metal oxide-based materials as advanced anodes for lithium-ion batteries, Nanoscale 4 (2012) 2526.

[109] K. Cao, T. Jin, L. Yang, L. Jiao, Recent progress in conversion reaction metal oxide anodes for Li-ion batteries, Mater. Chem. Front. 1 (2017) 2213.

[110] H. Tukamoto, A.R. West, Electronic conductivity of $LiCoO_2$ and its enhancement by magnesium doping, J. Electrochem. Soc. 144 (1997) 3164.

[111] M.S. Whittingham, Lithium batteries and cathode materials, Chem. Rev. 104 (2004) 4271.

[112] L.R. De Jesus, Y. Zhao, G.A. Horrocks, Justin L. Andrews, P. Stein, B.-X. Xu, S. Banerjee, Lithiation across interconnected V_2O_5 nanoparticle networks, J. Mater. Chem. A 5 (2017) 20141.

[113] J.L. Andrews, J. Cho, L. Wangoh, N. Suwandaratne, A. Sheng, S. Chauhan, K. Nieto, A. Mohr, K.J. Kadassery, M.R. Popeil, P.K. Thakur, M. Sfeir, D.C. Lacy, T.-L. Lee, P. Zhang, D.F. Watson, L.F.J. Piper, S. Banerjee, Hole extraction by design in photocatalytic architectures interfacing CdSe quantum dots with topochemically stabilized tin vanadium oxide, J. Am. Chem. Soc. 140 (2018) 17163.

[114] Y. Liu, W. Wang, X. Xu, J.-P. Marcel Veder, Z. Shao, Recent advances in anion-doped metal oxides for catalytic applications, J. Mater. Chem. A 7 (2019) 7280.

[115] M.B. Gawande, R.K. Pandey, R.V. Jayaram, Role of mixed metal oxides in catalysis science—versatile applications in organic synthesis, Catal. Sci. Technol. 2 (2012) 1113.

[116] Y. Wang, H. Arandiyan, J. Scott, A. Bagheri, H. Dai, R. Amal, Recent advances in ordered meso/macroporous metal oxides for heterogeneous catalysis: a review, J. Mater. Chem. A 5 (2017) 8825.

[117] L. Whittaker, H. Zhang, S. Banerjee, VO_2 nanosheets exhibiting a well-defined metal–insulator phase transition, J. Mater. Chem. 19 (2009) 2968.

[118] L. Whittaker, C. Jaye, Z. Fu, D.A. Fischer, S. Banerjee, Depressed phase transition in solution-grown VO_2 nanostructures, J. Am. Chem. Soc. 131 (2009) 8884.

[119] L. Whittaker, J.M. Velazquez, S. Banerjee, A VO-seeded approach for the growth of star-shaped VO_2 and V_2O_5 nanocrystals: facile synthesis, structural characterization, and elucidation of electronic structure, CrystEngComm 13 (2011) 5328.

[120] L. Whittaker, T.-L. Wu, A. Stabile, G. Sambandamurthy, S. Banerjee, Single-nanowire Raman microprobe studies of doping-, temperature-, and voltage-induced metal–insulator transitions of $W_xV_{1-x}O_2$ nanowires, ACS Nano 5 (2011) 8861.

[121] L. Whittaker, C.J. Patridge, S. Banerjee, Microscopic and nanoscale perspective of the metal–insulator phase transitions of VO_2: some new twists to an old tale, J. Phys. Chem. Lett. 2 (2011) 745–758.

[122] L. Whittaker, T.-L. Wu, C.J. Patridge, G. Sambandamurthy, S. Banerjee, Distinctive finite size effects on the phase diagram and metal–insulator transitions of tungsten-doped vanadium(iv) oxide, J. Mater. Chem. 21 (2011) 5580.

[123] N.A. Fleer, K.E. Pelcher, K. Nieto, E.J. Braham, J. Zou, G.A. Horrocks, Y. Naoi, S. W. Depner, B.J. Schultz, J. Amano, D.G. Sellers, S. Banerjee, Elucidating the crystallite size dependence of the thermochromic properties of nanocomposite VO_2 thin films, ACS Omega 3 (2018) 14280.

[124] P. Schulz, L.L. Whittaker-Brooks, B.A. MacLeod, D.C. Olson, Y.-L. Loo, A. Kahn, Electronic level alignment in inverted organometal perovskite solar cells, Adv. Mater. Interfaces 2 (2015) 1400532.

[125] A. Pérez-Tomás, A. Mingorance, D. Tanenbaum, M. Lira-Cantú, Chapter 8 – Metal oxides in photovoltaics: all-oxide, ferroic, and perovskite solar cells, in: M. Lira-Cantu (Ed.), The future of Semiconductor Oxides in Next-generation Solar Cells, Elsevier, 2018, p. 267.

[126] S. Rühle, A.Y. Anderson, H.-N. Barad, B. Kupfer, Y. Bouhadana, E. Rosh-Hodesh, A. Zaban, All-oxide photovoltaics, J. Phys. Chem. Lett. 3 (2012) 3755.

[127] T. Gershon, Metal oxide applications in organic-based photovoltaics, Mater. Sci. Technol. 27 (2011) 1357.

[128] I. Concina, Z.H. Ibupoto, A. Vomiero, Semiconducting metal oxide nanostructures for water splitting and photovoltaics, Adv. Energy Mater. 7 (2017) 1700706.

[129] S. Cho, J.-W. Jang, K.-H. Lee, J.S. Lee, Research update: strategies for efficient photoelectrochemical water splitting using metal oxide photoanodes, APL Mater. 2 (2014) 010703.

[130] N.K. Awad, E.A. Ashour, N.K. Allam, Recent advances in the use of metal oxide-based photocathodes for solar fuel production, J. Renewable Sustainable Energy 6 (2014) 022702.

[131] Y. Yang, S. Niu, D. Han, T. Liu, G. Wang, Y. Li, Progress in developing metal oxide nanomaterials for photoelectrochemical water splitting, Adv. Energy Mater. 7 (2017) 1700555.

[132] S. Kawasaki, R. Takahashi, T. Yamamoto, M. Kobayashi, H. Kumigashira, J. Yoshinobu, F. Komori, A. Kudo, M. Lippmaa, Photoelectrochemical water splitting enhanced by self-assembled metal nanopillars embedded in an oxide semiconductor photoelectrode, Nat. Commun. 7 (2016) 11818.

[133] D.K. Lee, D. Lee, M.A. Lumley, K.-S. Choi, Progress on ternary oxide-based photoanodes for use in photoelectrochemical cells for solar water splitting, Chem. Soc. Rev. 48 (2019) 2126.

[134] K. Sivula, Metal oxide photoelectrodes for solar fuel production, surface traps, and catalysis, J. Phys. Chem. Lett. 4 (2013) 1624.

[135] L. Alibabaei, H. Luo, R.L. House, P.G. Hoertz, R. Lopez, T.J. Meyer, Applications of metal oxide materials in dye sensitized photoelectrosynthesis cells for making solar fuels: let the molecules do the work, J. Mater. Chem. A 1 (2013) 4133.

[136] Z. Zhang, J. Liu, J. Gu, L. Su, L. Cheng, An overview of metal oxide materials as electrocatalysts and supports for polymer electrolyte fuel cells, Energy Environ. Sci. 7 (2014) 2535.

[137] Y. Zhou, X. Ye, J. Li, Z. Zhan, S. Wang, Metal-supported solid oxide fuel cells with a simple structure, J. Electrochem. Soc. 161 (2014) F332.

[138] V.V. Krishnan, Recent developments in metal-supported solid oxide fuel cells, Wiley Interdiscip, Rev. Energy Environ. 6 (2017) e246.

[139] N. Mahato, A. Banerjee, A. Gupta, S. Omar, K. Balani, Progress in material selection for solid oxide fuel cell technology: A review, Prog. Mater. Sci. 72 (2015) 141.

[140] A. Llordés, G. Garcia, J. Gazquez, D.J. Milliron, Tunable near-infrared and visible-light transmittance in nanocrystal-in-glass composites, Nature 500 (2013) 323.

[141] Z. Liu, Y. Zhong, I. Shafei, R. Borman, S. Jeong, J. Chen, Y. Losovyj, X. Gao, N. Li, Y. Du, E. Sarnello, T. Li, D. Su, W. Ma, X. Ye, Tuning infrared plasmon resonances in doped metal-oxide nanocrystals through cation-exchange reactions, Nat. Commun. 10 (2019) 1394.

[142] A. Figuerola, A. Fiore, R. Di Corato, A. Falqui, C. Giannini, E. Micotti, A. Lascialfari, M. Corti, R. Cingolani, T. Pellegrino, P.D. Cozzoli, L. Manna, One-pot synthesis and characterization of size-controlled bimagnetic FePt-iron oxide heterodimer nanocrystals, J. Am. Chem. Soc. 130 (2008) 1477.

[143] K.-W. Kwon, M. Shim, γ-Fe_2O_3/II–VI sulfide nanocrystal heterojunctions, J. Am. Chem. Soc. 127 (2005) 10269.

[144] H. Gu, Z. Yang, J. Gao, C.K. Chang, B. Xu, Heterodimers of Nanoparticles: Formation at a liquid–liquid interface and particle-specific surface modification by functional molecules, J. Am. Chem. Soc. 127 (2005) 34.

[145] L. Lartigue, D. Alloyeau, J. Kolosnjaj-Tabi, Y. Javed, P. Guardia, A. Riedinger, C. Péchoux, T. Pellegrino, C. Wilhelm, F. Gazeau, Biodegradation of iron oxide nanocubes: high-resolution in situ monitoring, ACS Nano 7 (2013) 3939.

[146] E.M. Shapiro, Biodegradable, polymer encapsulated, metal oxide particles for MRI-based cell tracking, Magn. Reson. Med. 73 (2015) 376.

[147] M.R. Hoffmann, S.T. Martin, W. Choi, D.W. Bahnemann, Environmental applications of semiconductor photocatalysis, Chem. Rev. 95 (1995) 69.

[148] Y. Wan, C. Samundsett, J. Bullock, M. Hettick, T. Allen, D. Yan, J. Peng, Y. Wu, J. Cui, A. Javey, A. Cuevas, Conductive and stable magnesium oxide electron-selective contacts for efficient silicon solar cells, Adv. Energy Mater. 7 (2017) 1601863.

[149] X. Yang, S. Zhang, Q. Yu, L. Zhao, P. Sun, T. Wang, F. Liu, X. Yan, Y. Gao, X. Liang, S. Zhang, G. Lu, One step synthesis of branched SnO_2/ZnO heterostructures and their enhanced gas-sensing properties, Sens. Actuators: B 281 (2019) 415.

[150] D. Zhao, P. Yang, N. Melosh, J. Feng, B.F. Chmelka, G.D. Stucky, Continuous mesoporous silica films with highly ordered large pore structures, Adv. Mater. 10 (1998) 1380.

[151] L.G. Gerling, S. Mahato, A. Morales-Vilches, G. Masmitja, P. Ortega, C. Voz, R. Alcubilla, J. Puigdollers, Transition metal oxides as hole-selective contacts in silicon heterojunctions solar cells, Sol. Energy Mater. Sol. Cells 145 (2016) 109.

[152] C. Battaglia, X. Yin, M. Zheng, I.D. Sharp, T. Chen, S. McDonnell, A. Azcatl, C. Carraro, B. Ma, R. Maboudian, R.M. Wallace, A. Javey, Hole selective MoO_x contact for silicon solar cells, Nano Lett. 14 (2014) 967.

[153] X. Yang, J. Guo, Y. Zhang, W. Liu, Y. Sun, Hole-selective NiO: Cu contact for NiO/Si heterojunction solar cells, J. Alloys Compd. 747 (2018) 563.

[154] A.H. Berg, G.S. Sahasrabudhe, R.A. Kerner, B.P. Rand, J. Schwartz, J.C. Sturm, Electron-blocking NiO/crystalline n-Si heterojunction formed by ALD at 175 °C, in: 2016 74th Annual Device Research Conference (DRC), 2016, pp. 1–2.

[155] H.-D. Um, N. Kim, K. Lee, I. Hwang, J.H. Seo, K. Seo, Dopant-free all-back-contact Si nanohole solar cells using MoO_x and LiF films, Nano Lett. 16 (2016) 981.

[156] G. Masmitjà, L.G. Gerling, P. Ortega, J. Puigdollers, I. Martín, C. Voz, R. Alcubilla, V_2O_x-based hole-selective contacts for c-Si interdigitated back-contacted solar cells, J. Mater. Chem. A 5 (2017) 9182.

[157] J. Geissbühler, J. Werner, S. Martin de Nicolas, L. Barraud, A. Hessler-Wyser, M. Despeisse, S. Nicolay, A. Tomasi, B. Niesen, S. De Wolf, C. Ballif, 22.5% efficient silicon heterojunction solar cell with molybdenum oxide hole collector, Appl. Phys. Lett. 107 (2015) 081601.

[158] J. Gan, V. Venkatachalapathy, B.G. Svensson, E.V. Monakhov, Influence of target power on properties of CuxO thin films prepared by reactive radio frequency magnetron sputtering, Thin Solid Films 594 (2015) 250.

[159] K. Bergum, H.N. Riise, S. Gorantla, P.F. Lindberg, I.J.T. Jensen, A.E. Gunnæs, A. Galeckas, S. Diplas, B.G. Svensson, E. Monakhov, Improving carrier transport in Cu_2O thin films by rapid thermal annealing, J. Phys.: Condens. Matter 30 (2018) 075702.

[160] Ø. Nordseth, R. Kumar, K. Bergum, L. Fara, C. Dumitru, D. Craciunescu, F. Dragan, I. Chilibon, E. Monakhov, E.S. Foss, G.B. Svensson, Metal oxide thin-film heterojunctions for photovoltaic applications, Materials 11 (2018).

[161] Y. Takiguchi, S. Miyajima, Device simulation of cuprous oxide heterojunction solar cells, Jpn. J. Appl. Phys. 54 (2015) 112303.

[162] F. Wang, N.K. Subbaiyan, Q. Wang, C. Rochford, G. Xu, R. Lu, A. Elliot, F. D'Souza, R. Hui, J. Wu, Development of nanopatterned fluorine-doped tin oxide electrodes for dye-sensitized solar cells with improved light trapping, ACS Appl. Mater. Interfaces 4 (2012) 1565.

[163] Z. Yin, J. Wei, Q. Zheng, Interfacial materials for organic solar cells: Recent advances and perspectives, Adv. Sci. 3 (2016) 1500362.

[164] Q. Kang, B. Yang, Y. Xu, B. Xu, J. Hou, Printable MoO_x anode interlayers for organic solar cells, Adv. Mater. 30 (2018) 1801718.

[165] Z. He, C. Zhong, S. Su, M. Xu, H. Wu, Y. Cao, Enhanced power-conversion efficiency in polymer solar cells using an inverted device structure, Nat. Photonics 6 (2012) 591.

[166] F. Cheng, Y. Wu, Y. Shen, X. Cai, L. Li, Enhancing the performance and stability of organic solar cells using solution processed MoO_3 as hole transport layer, RSC Adv. 7 (2017) 37952.

[167] W.J.E. Beek, M.M. Wienk, M. Kemerink, X. Yang, R.A.J. Janssen, Hybrid zinc oxide conjugated polymer bulk heterojunction solar cells, J. Phys. Chem. B 109 (2005) 9505.

[168] A.K.K. Kyaw, D.H. Wang, V. Gupta, J. Zhang, S. Chand, G.C. Bazan, A.J. Heeger, Efficient solution-processed small-molecule solar cells with inverted structure, Adv. Mater. 25 (2013) 2397.

[169] I. Jeon, S. Zeljkovic, K. Kondo, M. Yoshizawa, Y. Matsuo, Interface engineering of metal oxides using ammonium anthracene in inverted organic solar cells, ACS Appl. Mater. Interfaces 8 (2016) 29866.

[170] L. Guo, S. Yang, C. Yang, P. Yu, J. Wang, W. Ge, G.K.L. Wong, Highly monodisperse polymer-capped ZnO nanoparticles: preparation and optical properties, Appl. Phys. Lett. 76 (2000) 2901.

[171] J.J. Cavaleri, D.E. Skinner, D.P. Colombo, R.M. Bowman, Femtosecond study of the size-dependent charge carrier dynamics in ZnO nanocluster solutions, J. Chem. Phys. 103 (1995) 5378.

[172] E. Edri, S. Kirmayer, D. Cahen, G. Hodes, High open-circuit voltage solar cells based on organic–inorganic lead bromide perovskite, J. Phys. Chem. Lett. 4 (2013) 897.

[173] S. Sun, T. Salim, N. Mathews, M. Duchamp, C. Boothroyd, G. Xing, T.C. Sum, Y. M. Lam, The origin of high efficiency in low-temperature solution-processable bilayer organometal halide hybrid solar cells, Energy Environ. Sci. 7 (2014) 399.

[174] P.P. Boix, K. Nonomura, N. Mathews, S.G. Mhaisalkar, Current progress and future perspectives for organic/inorganic perovskite solar cells, Mater. Today 17 (2014) 16.

[175] Z. Li, T.R. Klein, D.H. Kim, M. Yang, J.J. Berry, M.F.A.M. van Hest, K. Zhu, Scalable fabrication of perovskite solar cells, Nat. Rev. Mater. 3 (2018) 18017.

[176] G. Grancini, M.K. Nazeeruddin, Dimensional tailoring of hybrid perovskites for photovoltaics, Nat. Rev. Mater. 4 (2019) 4.

[177] J. Huang, Y. Yuan, Y. Shao, Y. Yan, Understanding the physical properties of hybrid perovskites for photovoltaic applications, Nat. Rev. Mater. 2 (2017) 17042.

[178] J.M. Ball, A. Petrozza, Defects in perovskite-halides and their effects in solar cells, Nat. Energy 1 (2016) 16149.

[179] S.D. Stranks, G.E. Eperon, G. Grancini, C. Menelaou, M.J.P. Alcocer, T. Leijtens, L.M. Herz, A. Petrozza, H.J. Snaith, Electron-hole diffusion lengths exceeding 1 micrometer in an organometal trihalide perovskite absorber, Science 342 (2013) 341.

[180] Y. Bai, X. Meng, S. Yang, Interface engineering for highly efficient and stable planar p-i-n perovskite solar cells, Adv. Energy Mater. 8 (2018) 1701883.

[181] Z. Liu, J. Chang, Z. Lin, L. Zhou, Z. Yang, D. Chen, C. Zhang, S. Liu, Y. Hao, High-performance planar perovskite solar cells using low temperature, solution–combustion-based nickel oxide hole transporting layer with efficiency exceeding 20%, Adv. Energy Mater. 8 (2018) 1703432.

[182] W. Chen, Y. Wu, J. Fan, A.B. Djurišić, F. Liu, H.W. Tam, A. Ng, C. Surya, W.K. Chan, D. Wang, Z.-B. He, Understanding the doping effect on NiO: toward high-performance inverted perovskite solar cells, Adv. Energy Mater. 8 (2018) 1703519.

[183] J. Tang, D. Jiao, L. Zhang, X. Zhang, X. Xu, C. Yao, J. Wu, Z. Lan, High-performance inverted planar perovskite solar cells based on efficient hole-transporting layers from well-crystalline NiO nanocrystals, Sol. Energy 161 (2018) 100.

[184] Z. Liu, A. Zhu, F. Cai, L. Tao, Y. Zhou, Z. Zhao, Q. Chen, Y.-B. Cheng, H. Zhou, Nickel oxide nanoparticles for efficient hole transport in p-i-n and n-i-p perovskite solar cells, J. Mater. Chem. A 5 (2017) 6597.

[185] X. Liu, J. Iocozzia, Y. Wang, X. Cui, Y. Chen, S. Zhao, Z. Li, Z. Lin, Noble metal–metal oxide nanohybrids with tailored nanostructures for efficient solar energy conversion, photocatalysis and environmental remediation, Energy Environ. Sci. 10 (2017) 402.

[186] M. Abb, Y. Wang, N. Papasimakis, C.H. de Groot, O.L. Muskens, Surface-enhanced infrared spectroscopy using metal oxide plasmonic antenna arrays, Nano Lett. 14 (2014) 346.

[187] G. Demirel, H. Usta, M. Yilmaz, M. Celik, H.A. Alidagi, F. Buyukserin, Surface-enhanced Raman spectroscopy (SERS): an adventure from plasmonic metals to organic semiconductors as SERS platforms, J. Mater. Chem. C 6 (2018) 5314.

[188] M.Z. Ghori, S. Veziroglu, A. Hinz, B.B. Shurtleff, O. Polonskyi, T. Strunskus, J. Adam, F. Faupel, O.C. Aktas, Role of UV plasmonics in the photocatalytic performance of TiO_2 decorated with aluminum nanoparticles, ACS Appl. Nano Mater. 1 (2018) 3760.

[189] R.W. Johns, H.A. Bechtel, E.L. Runnerstrom, A. Agrawal, S.D. Lounis, D.J. Milliron, Direct observation of narrow mid-infrared plasmon linewidths of single metal oxide nanocrystals, Nat. Commun. 7 (2016) 11583.

[190] M. Kanehara, H. Koike, T. Yoshinaga, T. Teranishi, Indium tin oxide nanoparticles with compositionally tunable surface plasmon resonance frequencies in the near-IR region, J. Am. Chem. Soc. 131 (2009) 17736.

[191] R. Haldavnekar, K. Venkatakrishnan, B. Tan, Non plasmonic semiconductor quantum SERS probe as a pathway for in vitro cancer detection, Nat. Commun. 9 (2018) 3065.

[192] H.-Y. Shin, E.-L. Shim, Y.-J. Choi, J.-H. Park, S. Yoon, Giant enhancement of the Raman response due to one-dimensional ZnO nanostructures, Nanoscale 6 (2014) 14622.

[193] B.Y. Zhang, A. Zavabeti, A.F. Chrimes, F. Haque, L.A. O'Dell, H. Khan, N. Syed, R. Datta, Y. Wang, A.S.R. Chesman, T. Daeneke, K. Kalantar-Zadeh, J.Z. Ou, Degenerately hydrogen doped molybdenum oxide nanodisks for ultrasensitive plasmonic biosensing, Adv. Funct. Mater. 28 (2018) 1706006.

[194] M.Y. Kuo, J.Y. Hsing, T.T. Chiu, C.N. Li, W.T. Kuo, T.S. Lay, M.H. Shih, Quantum efficiency enhancement in selectively transparent silicon thin film solar cells by distributed Bragg reflectors, Opt. Express 20 (2012) A828.

[195] N. Feng, J. Michel, L. Zeng, J. Liu, C. Hong, L.C. Kimerling, X. Duan, Design of highly efficient light-trapping structures for thin-film crystalline silicon solar cells, IEEE Trans. Electron Devices 54 (2007) 1926.

[196] L. Zhao, Y.H. Zuo, C.L. Zhou, H.L. Li, H.W. Diao, W.J. Wang, A highly efficient light-trapping structure for thin-film silicon solar cells, Sol. Energy 84 (2010) 110.

[197] X. Sheng, S.G. Johnson, L.Z. Broderick, J. Michel, L.C. Kimerling, Integrated photonic structures for light trapping in thin-film Si solar cells, Appl. Phys. Lett. 100 (2012) 111110.

[198] A. Tukiainen, A. Aho, V. Polojärvi, M. Guina, Improving the current output of GaInNAs solar cells using distributed Bragg reflectors, in: 2016 IEEE 43rd Photovoltaic Specialists Conference (PVSC), 2016, p. 0368.

[199] W.J. Nimens, L. Whittaker-Brooks, M.H. Bartl, Enhanced sensing in mixed porous–solid photonic stacks, J. Mater. Chem. C 4 (2016) 668.

[200] R.M. De La Rue, C. Seassal, Photonic crystal devices: some basics and selected topics, Laser Photonics Rev. 6 (2012) 564.

[201] J. Zhao, Calculation of photonic band-gap of one dimensional photonic crystal, J. Phys.: Conf. Ser. 183 (2009) 012018.

[202] A. Lakhtakia, R.J. Martín-Palma, Engineered Biomimicry, Waltham, Elsevier, MA, 2013.

[203] E. Yablonovitch, Photonic crystals: semiconductors of light, Sci. Am. 285 (2001) 47.

[204] M. Barhoum, J. Morrill, D. Riassetto, M. Bartl, Rapid sol–gel fabrication of high-quality thin-film stacks on planar and curved substrates, Chem. Mater. 23 (2011) 5177.
[205] Fink, Winn, Fan, Chen, Michel, Joannopoulos, Thomas, A dielectric omnidirectional reflector, Science (New York, N.Y.) 282 (1998) 1679.
[206] H.-Y. Lee, T. Yao, Design and evaluation of omnidirectional one-dimensional photonic crystals, J. Appl. Phys. 93 (2003) 819.
[207] R.M. Almeida, A.S. Rodrigues, Photonic bandgap materials and structures by sol–gel processing, J. Non-Cryst. Solids 326–327 (2003) 405.
[208] F. Giorgis, Optical microcavities based on amorphous silicon–nitride Fabry-Pérot structures, Appl. Phys. Lett. 77 (2000) 522.
[209] N. Tessler, R. Nagar, G. Eisenstein, J. Salzman, U. Koren, G. Raybon, C.A. Burns, Distributed Bragg reflector active optical filters, IEEE J. Quantum Electron. 27 (1991) 2016.
[210] K. Wu, Z. Li, J. Guo, Y. Xiao, H. Qi, W. Dong, S. Ruan, W. Chen, Y. Chen, Design of thermo-optic tunable optical filter based on Si/Air DBR and polymer Fabry-Perot microcavity in SOI, Optik 125 (2014).
[211] M.W. Pruessner, T.H. Stievater, J.B. Khurgin, W.S. Rabinovich, Integrated waveguide-DBR microcavity optomechanical system, Opt. Express 19 (2011) 21904.
[212] Y. Lu, R. Ganguli, C.A. Drewien, M.T. Anderson, C.J. Brinker, W. Gong, Y. Guo, H. Soyez, B. Dunn, M.H. Huang, J.I. Zink, Continuous formation of supported cubic and hexagonal mesoporous films by sol–gel dip-coating, Nature 389 (1997) 364.
[213] C. Lei, D.G. Deppe, Optical gain enhancement in Fabry-Perot microcavity lasers, J. Appl. Phys. 71 (1992) 2530.
[214] J. Bellessa, S. Rabaste, J.C. Plenet, J. Dumas, J. Mugnier, O. Marty, Eu^{3+}-doped microcavities fabricated by sol–gel process, Appl. Phys. Lett. 79 (2001) 2142.
[215] I.B. Burgess, N. Koay, K.P. Raymond, M. Kolle, M. Lončar, J. Aizenberg, Wetting in color: colorimetric differentiation of organic liquids with high selectivity, ACS Nano 6 (2012) 1427.
[216] K.P. Raymond, I.B. Burgess, M.H. Kinney, M. Lonar, J. Aizenberg, Combinatorial wetting in colour: an optofluidic nose, Lab Chip 12 (2012) 3666.
[217] V.N. Konopsky, T. Karakouz, E.V. Alieva, C. Vicario, S.K. Sekatskii, G. Dietler, Photonic crystal biosensor based on optical surfacewaves, Sensors (Switzerland) 13 (2013) 2566.
[218] Z. Alothman, A review: fundamental aspects of silicate mesoporous materials, Materials 5 (2012) 2874.
[219] V. Pore, M. Ritala, M. Leskelä, S. Areva, M. Järn, J. Järnström, H_2S modified atomic layer deposition process for photocatalytic TiO_2 thin films, J. Mater. Chem. 17 (2007) 1361.
[220] M.N.R. Ashfold, P.W. May, C.A. Rego, N.M. Everitt, Thin film diamond by chemical vapour deposition methods, Chem. Soc. Rev. 23 (1994) 21.
[221] M.M. Hawkeye, M.J. Brett, Optimized colorimetric photonic-crystal humidity sensor fabricated using glancing angle deposition, Adv. Funct. Mater. 21 (2011) 3652.
[222] Janssen Cowern, G. van de Walle, Gravesteijn, Impurity diffusion via an intermediate species: the B-Si system, Phys. Rev. Lett. 65 (1990) 2434.
[223] X. Wang, Z. Feng, J. Shi, G. Jia, S. Shen, J. Zhou, C. Li, Trap states and carrier dynamics of $TiO_{(2)}$ studied by photoluminescence spectroscopy under weak excitation condition, Phys. Chem. Chem. Phys. 12 (2010) 7083.
[224] S.Y. Choi, M. Mamak, G. von Freymann, N. Chopra, G.A. Ozin, Mesoporous Bragg stack color tunable sensors, Nano Lett. 6 (2006) 2456.
[225] M.R. Dahlby, M. Barhoum, M.H. Bartl, Sol–gel-derived thin-film stacks with high radiation stability, Thin Solid Films 562 (2014) 435.
[226] P.A. Snow, E.K. Squire, P.S.J. Russell, L.T. Canham, Vapor sensing using the optical properties of porous silicon Bragg mirrors, J. Appl. Phys. 86 (1999) 1781.
[227] I. Pavlichenko, A.T. Exner, M. Guehl, P. Lugli, G. Scarpa, B.V. Lotsch, Humidity-enhanced thermally tunable TiO_2/SiO_2 Bragg stacks, J. Phys. Chem. C 116 (2012) 298.
[228] J. Kobler, B.V. Lotsch, G.A. Ozin, T. Bein, Vapor-sensitive bragg mirrors and optical isotherms from mesoporous nanoparticle suspensions, ACS Nano 3 (2009) 1669.
[229] P.C.A. Alberius, K.L. Frindell, R.C. Hayward, E.J. Kramer, G.D. Stucky, B.F. Chmelka, General predictive syntheses of cubic, hexagonal, and lamellar silica and titania mesostructured thin films, Chem. Mater. 14 (2002) 3284.
[230] S.M. Weiss, H. Ouyang, J. Zhang, P.M. Fauchet, Electrical and thermal modulation of silicon photonic bandgap microcavities containing liquid crystals, Opt. Express 13 (2005) 1090.
[231] M.C. Fuertes, F.J. López-Alcaraz, M.C. Marchi, H.E. Troiani, V. Luca, H. Míguez, G.J.A.A. Soler-Illia, Photonic crystals from ordered mesoporous thin-film functional building blocks, Adv. Funct. Mater. 17 (2007) 1247.
[232] I.G. Kolobov, W.B. Euler, I.A. Levitsky, Optical humidity sensing and ultrasound effect for mesoporous silicon one-dimensional photonic crystals, Appl. Opt. 49 (2010) 137.
[233] S. Colodrero, M. Ocaña, A.R. González-Elipe, H. Míguez, Response of nanoparticle-based one-dimensional photonic crystals to ambient vapor pressure, Langmuir 24 (2008) 9135.
[234] S. Colodrero, M. Ocaña, H. Míguez, Nanoparticle-based one-dimensional photonic crystals, Langmuir 24 (2008) 4430.
[235] S. Guldin, M. Kolle, M. Stefik, R. Langford, D. Eder, U. Wiesner, U. Steiner, Tunable mesoporous Bragg reflectors based on block-copolymer self-assembly, Adv. Mater. 23 (2011) 3664.
[236] M.N. Ghazzal, O. Deparis, J. De Coninck, E.M. Gaigneaux, Tailored refractive index of inorganic mesoporous mixed-oxide Bragg stacks with bio-inspired hygrochromic optical properties, J. Mater. Chem. C 1 (2013) 6202.